UNIVERSITEIT GENT

FACULTY OF ENGINEERING AND ARCHITECTURE

MASTER'S DISSERTATION

MASTER OF SCIENCE IN ELECTRICAL ENGINEERING

# Coupled Oscillator Phased Antenna Array Element for Phase Shifter-less Beam Steering

Luca Montero Bayo

**Supervisors**

Prof. dr. ir. Dries Vande Ginste, Prof. dr. ir. Hendrik Rogier

**Counselors**

Ir. Martijn Huynen, Ing. Quinten Van den Brande

—

Faculty of Engineering and Architechture

Ghent University, 2017-2018

# Contents

# Chapter 1

# Introduction

The ubiquity of modern wireless communications and the huge and ever-growing demand of data bandwidth are accelerating the development of technologies operating at higher frequencies, due to the high congestion of the currently used frequency spectrum. Nonetheless, these new high frequency bands (such as the millimeter-wave band, a well-established candidate for 5G) face a hostile propagation channel, where an increased path loss, together with critical shadowing and multipath effects, pose challenges for future communication systems.

To overcome these problems, a lot of attention has been put on antenna arrays, which produce high directivity with steerable beam direction. This topology can be currently found in numerous applications, such as radar, astronomy or satellite communications, where a high-throughput directive beam is usually needed. Furthermore, beam-scanning ability is being increasingly required for high mobility scenarios, like aircraft or low-orbit satellite links, where transmitting and/or receiving antennas can potentially move at fast speeds.

Overall, the ability to obtain a steerable focused beam is advantageous for many applications. Applied to current communication systems, it can dramatically reduce interference among technologies co-existing in the same band, as well as improve power efficiency, by connecting the antenna directly to a targeted user.

However, conventional beam-forming schemes rely on bulky and costly components, with little applicability for higher microwave frequencies. Traditional phase shifter-based arrays, which account for the currently most widespread beam-forming technique, are losing pop-

ularity for future applications, where system cost-effectiveness is strongly embraced. Phase control of the individual elements of an array is done by as many phase shifters as passive elements in the array, which causes high costs and high insertion losses that can no longer be ignored.

Research on technologies for beam-steerable tunable devices is attracting ample interest, promoting high performance and low manufacturing costs in order to obtain viable widespread solutions. In applications where a broad steering range is not paramount, coupled oscillator arrays operating under the injection-locking principle represent a promising alternative to mitigate some of the current drawbacks.

The goal of this master's dissertation is to design and manufacture an array element, part of a beam steering network controlled by coupled oscillators. The complete system will consist of an efficient, dedicated antenna array compactly integrated with coupled oscillators, which will be explained in Chapter 2. A single antenna element and oscillator will be co-designed to achieve optimal characteristics. The operating principle and optimized simulation results of the antenna and oscillator modules will be described in Chapter 3 and Chapter 4, respectively. Next, in Chapter 5, manufactured prototypes and measurement results to validate these simulations will be presented. Lastly, in Chapter 6, the conclusions will be formulated, together with the next steps required to come to a fully operational beam steering network.

# Chapter 2

# System Architecture

This master's dissertation will cover the design of an array element, that forms the basic antenna element of a phase-shifterless beamsteering antenna array operating at the 2.45 GHz-centered ISM (Industrial, Scientific and Medical) band. This chapter will provide an overview of the antenna array system architecture and discuss the operating principle of a coupled-oscillator based phase steering mechanism.

According to antenna array theory [1], a uniformly spaced array of isotropic antennas excited with a progressive phase shift ($\Delta\phi$) between adjacent elements will have its main lobe steered towards the $\theta_{scan}$ direction [2]. The phase difference between these elements can be expressed as:

$$\Delta\phi = \frac{2\pi d}{\lambda} \sin\left(\theta_{scan}\right). \tag{2.1}$$

where $d$ corresponds to the spacing between subsequent antenna phase centers, usually set to $\lambda/2$ to avoid the generally undesired grating lobes[1]. To provide this excitation scheme, a single-source feeding network with analog or digitally-controlled phase shifters is normally used. Nevertheless, the large footprint of these components, their substantial losses at high frequencies and the large cost make this approach unattractive for emerging applications. In order to overcome the drawbacks of conventional phased arrays, several techniques have been

[1]For an array with uniform amplitude, the closest unwanted grating lobe will not be visible when $\frac{d}{\lambda} < \frac{1}{1+\sin(|\theta_{scan}|)}$, so for full scan coverage ($|\theta_{scan}| < 90°$) $d$ is set to $\lambda/2$ [2].

investigated to eliminate the need for the phase shifter network components. Switched-beam, frequency-scanned or even mechanically scanned systems have been considered as solutions to the previously mentioned problems [3]. However, the use of a coupled oscillator array has recently surfaced as a noteworthy alternative [4].

## 2.1 Coupled Oscillator Phase Steering

The distribution of a constant phase difference between antenna elements with the use of coupled oscillators is based on the injection locking phenomenom [3], which takes advantage of the unconventional phase dynamics of nonlinear oscillators to obtain a controlled frequency and phase output. As it is thoroughly analyzed in [5], when a signal of frequency $w_{inj}$ is injected into an oscillator with free-running frequency of $w_{osc}$, the latter synchronizes to the injected signal. A steady-state solution can be found when the injected signal frequency is inside the locking range ($w_{osc} \pm \Delta w_L$). The locking range value ($2\Delta w_L$) is proportional to the injected signal amplitude, yet inversely proportional to the oscillator signal amplitude and Quality Factor (Q), but it always represents a phase difference of $\pm 90°$ between the oscillator's output and the injected signal at both edges of the locking range ($\pm\Delta w_L$) [6].

Several topologies that take advantage of injection-locked coupled oscillators have been investigated [3, 7], but most of them rely on the use of at least one phase shifter to obtain the desired phased array [8]. Fig. 2.1 illustrates the system architecture of the array proposed in this dissertation: a combination of Stephan's [9] and York's [10] beam-steering architectures, which entirely eliminates the use of phase shifters by means of a single-ended signal injection into an array of coupled oscillators.

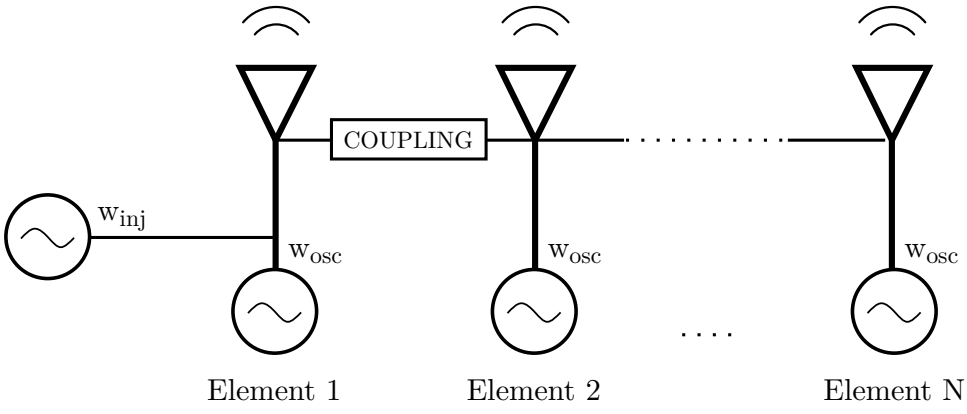


Figure 2.1: Block diagram representation of the coupled oscillator array system architecture.

In the system diagram depicted in Fig. 2.1, which operates in a similar way as the phased array presented in [10], an external oscillator injects a signal of frequency $w_{inj}$ into an oscillator at the edge of the array. The frequency of the oscillator in which the signal is being injected — namely, Element 1 — is synchronized with $w_{inj}$, and the phase difference between these oscillators would depend, among other things, on both signal strengths [5]. Then, precisely calculating nearest-neighbour bidirectional coupling between oscillators, this frequency and phase shift propagates throughout the array, eventually making a progressive phase difference between oscillators tangible and, as a result, a steerable antenna array. Unless additional mechanisms are used ([11]), phase difference between adjacent antenna elements is limited to $\Delta\phi < \pm 90°$. As defined by (2.1), scanning of this coupled oscillator array scheme will be constrained to a $|\theta_{scan}| < 30°$ steering angle.

Although quantitative performance results of this system can be analytically obtained [12] and the required signal amplitudes and coupling coefficients can be carefully calculated [13], the goal of this dissertation is the design of a single array element. However, the exploration of the entire system architecture is useful to determine the system requirements of each module of the array element, which will be described in Section 3.1 and 4.1.

## 2.2 Cost-effective Antenna Coupling Mechanism for Injection-locked Phased Oscillator Array

In order to obtain a controlled coupling between oscillators, several techniques, such as a resistive loaded microstrip line [14] or loosely coupled patch antennas [15], have been studied. Nevertheless, the use of high-Q cavities as resonators in the oscillator circuit has shown enhanced injection-locked synchronization in coupled oscillator arrays [16]. Substrate Integrated Technology (SIW) is particularly appropriate to design compact and low-cost cavities. In [17], an SIW cavity acting as a resonating load of an externally biased diode was used in the design of an oscillator. An SIW cavity was also used in [18], where the cavity was modelled by an external electromagnetic simulation to enable precise nonlinear simulation techniques and predict the oscillation frequency and output power. Furthermore, in cavity-loaded oscillators, cavity-backed antennas can be compactly integrated in the same SIW structure. This SIW-based active antennas have been proposed in [19, 20], where oscillator and antenna are integrated in opposite sides of a single-layer substrate.

Among the several advantages of SIW technology regarding oscillator design, the use

of SIW-based components to design beam-steering networks is getting increased attention [21, 22]. Although phase shifter-based feeding network to control an antenna phased array can be integrated in SIW technology [23], a SIW-based coupled oscillator array architecture for beam steering is proposed in [21], eliminating the need of phase shifters.

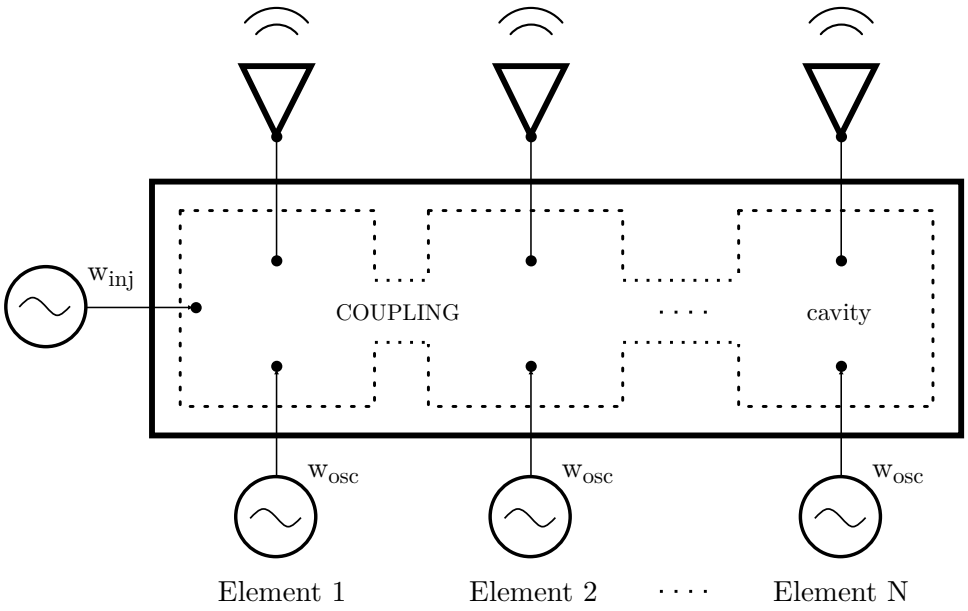


Figure 2.2: Cavity-coupled oscillator array architecture.

Inspired by the aforementioned developments on practical coupled oscillator array beam steering design, a more detailed schematic of the system architecture proposed in this dissertation is shown in Fig. 2.2. Based on active SIW cavity-backed antenna array elements, the coupling among the array to configure the injection-locked phase shift is controlled by appropriately tuning an aperture-based coupling between cavities. Using this coupling mechanism, 1D and 2D arrays can be synthesized configuring the intra-cavity coupling matrix. Besides, as opposed to microstrip-based coupling circuitry, aperture-coupled cavities do not generate undesired radiation, and the narrowband coupling enhances locking between oscillators, which is specially problematic in large injection-locked oscillator arrays [24].

Fig. 2.3 illustrates an array element of the architecture shown in Fig. 2.2. Each element is entirely integrated in a single SIW structure, where the cavity serves both as a high-Q resonating load for the oscillator and as a feeding structure for the radiating element. Active and radiating modules of this array element will be on opposite sides of the SIW

implementation, minimizing unwanted interference between both modules [21]. To design the array element depicted in Fig. 2.3, the design of the cavity-backed antenna module will be described in Chapter 3. Next, in Chapter 4, an oscillator will be co-designed for optimum integration with the antenna. The unavoidable dependance of the oscillator on the cavity-backed antenna impedance will set the basis for the co-design considerations taken in this dissertation.

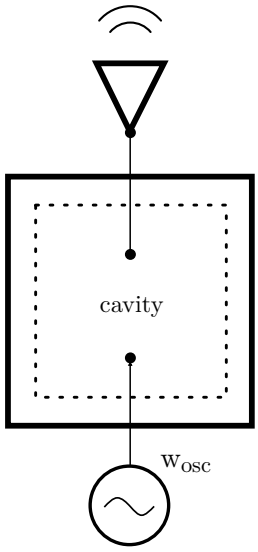


Figure 2.3: Phased Antenna Array Element

# Chapter 3

# Antenna Design

This chapter will cover the design process of the antenna, from realistic specifications to a final working prototype, starting with Section 3.1, where the antenna requirements are briefly listed. The chosen topology and the working principles are described in detail in Section 3.2 and Section 3.3, respectively. To conclude, Section 3.4 describes the implementation technology, gives final antenna dimensions and includes key simulation results of an optimized antenna prototype.

## 3.1 Design Requirements

The device operates in the 2.45 GHz-centered ISM band, which ranges from 2.4 to 2.5 GHz. Therefore, the reflection coefficient ($|S_{11}|$) — with respect to a 50Ω port impedance — must be optimized to a magnitude below −10 dB in this bandwidth. To diminish the influence of potential out-of-band interferers and for enhanced oscillator operation, the response of the antenna should be optimized to obtain a high Quality Factor. Considering the Q-factor is inversely proportional to the impedance bandwidth, narrowband operation is preferred. As such, the bandwidth should not exceed 50 MHz, corresponding to a Q = 49. To ensure a stable array gain in a broad range of steering angles for the antenna array, the design of the array element should aim for an omnidirectional radiation pattern in its positive hemisphere. Given the fact that the injection-locked phased antenna array has a 30° steering angle limitation, a half-power beamwidth of at least 60° should be achieved to ensure this gain stability. This intended radiation pattern implies minimum backside radiation, corresponding to a

high Front-to-Back Ratio (FTBR) of at least 10 dB. In addition, radiation efficiency should be maximized — preferably exceeding 85% — to obtain optimum gain.

Finally, to guarantee robustness and versatility in realistic scenarios, a mechanically reliable and low-cost fabrication process is embraced, aiming for a modular, thin-profile and lightweight implementation. Promoting seamless integration with transceiver components, while ensuring high shielding from undesired radiation, is recommended.

## 3.2 Antenna Topology

Slot antennas are commonly used due to their high efficiency and their suitability for thin profile transceivers. However, their bidirectional nature can be an obstacle when a slot antenna is placed close to conductive bodies or integrated in multilayered circuitry [25]. Cavity-backed antennas (CBA), which are characterized by a negligible backside radiation, have been widely investigated for their outstanding radiation performance and the benefits of their isolation from other components [26]. Consequently, CBAs have proven to be a suitable element in the design of large antenna arrays, given the negligible mutual coupling between the antenna elements [27]. Therefore, to satisfy the aforementioned design requirements, a cavity-backed slot antenna (CBSA) is the chosen topology.

As a result of cavity resonance, CBSAs are inherently narrowband [25]. In CBSAs, the walls confine the electromagnetic fields to the cavity and radiation is only generated from the slot with an omnidirectional radiation pattern. SIW is used as a fabrication technique for the CBSA in this dissertation, which retains the advantages of traditional high-efficiency, high-Q cavity-backed antennas with a low-cost, low-profile implementation [28].

## 3.3 Operation Principle

To explain the operating principle of a cavity-backed slot antenna, it is important to understand the underlying physics of this type of antennas. Slot antennas are narrow apertures that have been cut out of a metallic plane. In the same way that dipoles radiate based on an electric current distribution, slot antennas — which represent an electromagnetic dual problem — are excited with a magnetic current along the length of the gap in the conductor. To create this current, a magnetic source needs to be present, in the form of an electric field confined to the slot and perpendicular to this current (Fig. 3.1) [29].

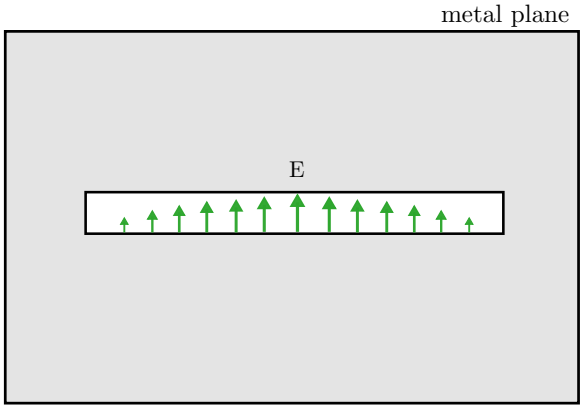


Figure 3.1: Excitation of a slot on a metal plane.

One efficient way to get this electric field is by taking advantage of the electromagnetic fields present in metallic cavities. Slots can be strategically placed in the walls of the cavities, such that the fields at that location are suitable for a correct excitation of the aperture. However, although there are countless possibilities, an intelligent way to determine an optimum position of a slot is by studying the electromagnetic fields that reside inside cavities and the effects of the presence of a slot in one of the walls.

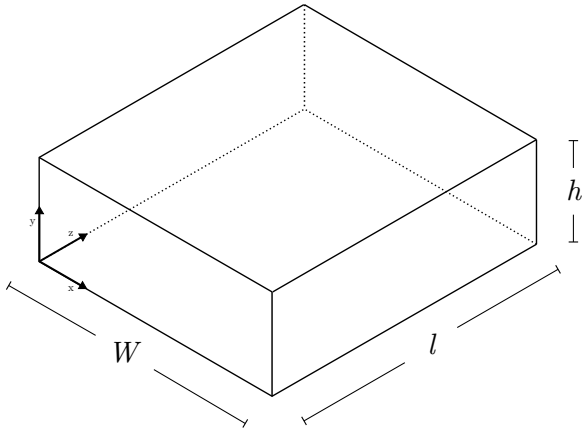


Figure 3.2: Cavity dimensions.

As it is comprehensively described in [30], rectangular cavities support an infinite number of TE (Transversal Electric) and TM (Transversal Magnetic) modes. When boundary conditions are applied, a vanishing tangential electric field is imposed at the conducting walls

of the cavity, and given the sinusoidal nature of field equations, these conditions are satisfied for a number of stationary fields in the $\hat{x}$, $\hat{y}$ and $\hat{z}$ directions. Therefore, these stationary fields only exist at those frequencies that make cavity dimensions (Fig. 3.2) an integer number of half-wavelengths. These so-called resonant frequencies are defined as:

$$f_{r_{mnp}} = \frac{1}{2\sqrt{\mu\varepsilon}}\sqrt{\left(\frac{m}{W}\right)^2 + \left(\frac{n}{h}\right)^2 + \left(\frac{p}{L}\right)^2}, \tag{3.1}$$

where indices $m$, $n$ and $p$ indicate the number of variations in the standing wave along cavity width ($W$), height ($h$) and length ($L$), respectively. When $h \ll W < L$, the first resonant mode is $\mathrm{TE}_{101}$. $\mathrm{TE}_{101}$ is characterized by the absence of $E_x$ and $E_z$ components, so the electric field is entirely defined by $E_y$ and depends on ($x$,$z$) coordinates. Indices $m = 1$ and $p = 1$ represent one half-sinusoidal cycle for both $\hat{x}$ and $\hat{z}$ axes, whereas $n = 0$ suggests no variation along $\hat{y}$. Typically used higher order modes are $\mathrm{TE}_{201}$ and $\mathrm{TE}_{102}$[1] [28], which present a complete sinusoidal cycle along $\hat{x}$ and $\hat{z}$, respectively. Electric field magnitude distribution for these resonant modes is shown in Fig. 3.3.

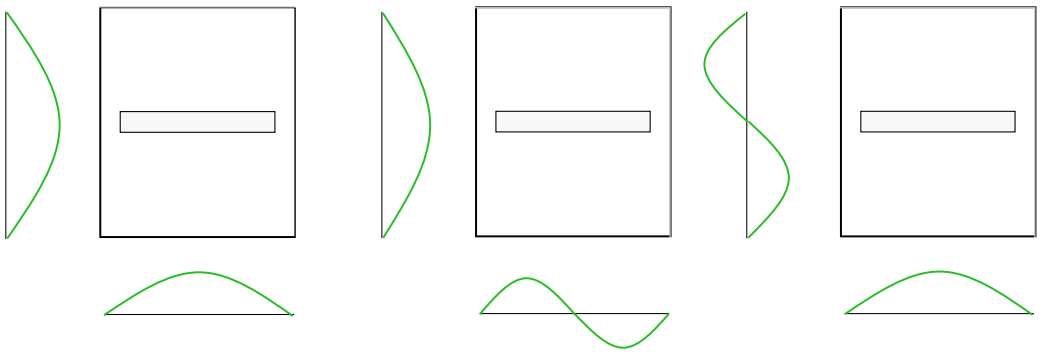

(a) Mode $\mathrm{TE}_{101}$ (b) Mode $\mathrm{TE}_{201}$ (c) Mode $\mathrm{TE}_{102}$

Figure 3.3: Electric field magnitude $|E_y|$ for different resonant modes.

Slots are usually placed in one of the sidewalls of a waveguide, perpendicular to $\hat{y}$ (Fig. 3.4a). This way, in monomode operation, the $E_y$ component of the propagating $\mathrm{TE}_{101}$ mode is confined to the slot — which is $\lambda/2$ long — and radiation can intuitively be seen as

[1]Based on the assumption that $h < W < L$, resonant modes with order index $n > 0$ appear at higher frequencies (1).

efficient leakage through it [29]. Nevertheless, some recently popularized fabrication technologies, such as SIW, present height limitations, so placing a slot in one of the sidewalls quickly becomes unwieldy.

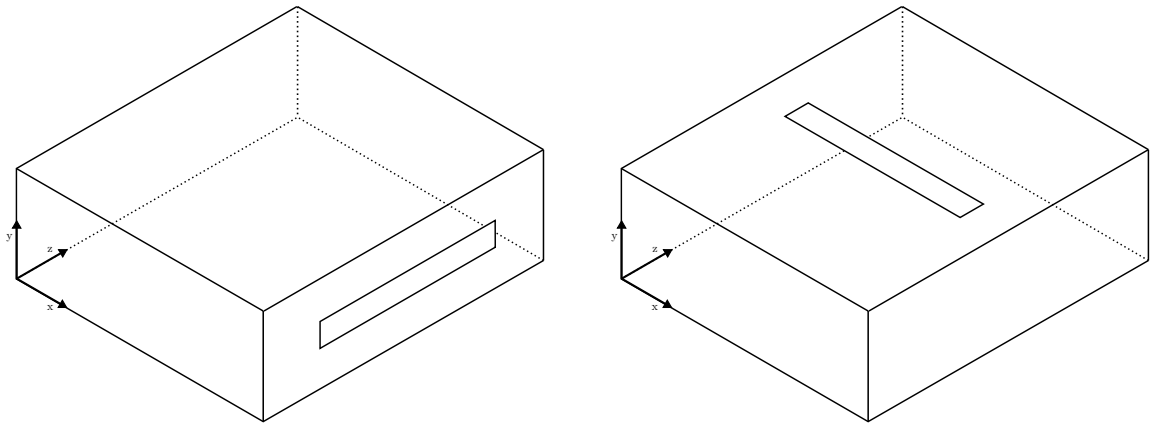

(a) Slot located at the center of a cavity sidewall ($x = W$)

(b) Slot located at the center of the cavity top wall ($y = h$)

Figure 3.4: Representation of different slot positions

The excitation of a slot that is placed in either the bottom ($y = 0$) or top ($y = h$) wall of the cavity (Fig. 3.4b) requires a different description, because no component of the electric field is tangent to the aperture. In this situation, the electric field generated inside the slot can be perceived as the result of a voltage difference between the long sides of the slot. This way, when $TE_{101}$ or $TE_{201}$ are present in the CBSA shown in Fig. 3.4b, there will be no such voltage difference and the slot will not be excited, that is to say, radiation efficiency will have a marginal value. However, if $TE_{102}$ is excited, the two halves generated by the slot in the middle of the cavity (Fig. 3.5) will be antiphase and a large voltage difference will effectively create a transverse electric field across the slot ($E_z$) so it can radiate [31].

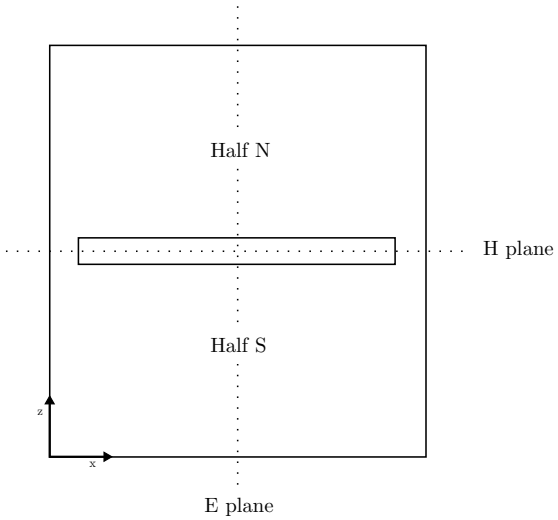


Figure 3.5: Representation of the two cavity halves at each side of the slot, for a slot placed at the center of the top wall ($y = h$).

Although it is meant to increase operating bandwidth, the working principle of the CBSA presented in [32] can still be used for narrowband designs. In this article, a hybrid mode — combination of $TE_{101}$ and $TE_{102}$ — is present in the cavity, thanks to a long nonresonant slot that is key to force this combination dividing the cavity in two parts, as depicted in Fig. 3.5. Two different field distributions can be accomplished with the combination of these modes. When there is a stronger $TE_{102}$ resonance, the electric fields in each of the halves are strongly out-of-phase, so successful radiation can be generated from the aperture with the highest radiation efficiency ($\eta_{rad}$). When $TE_{101}$ resonance is stronger, the fields in each part are in-phase, but with enough amplitude difference to induce a voltage difference in the slot. As a result, the use of a long nonresonant slot to combine different modes offers some flexibility to obtain the required electric field to feed the slot and enables $TE_{101}$ as a contributor to the operating field distribution.

## 3.4 Standalone Antenna Prototype

Substrate Integrated Waveguide technology has received special attention over the last years, as it provides a compact and lightweight alternative to conventional waveguides by using standard and low-cost printed circuit board (PCB) processes [21]. As a result, low-profile SIW

cavity-backed antennas have been studied with different configurations and feeding techniques [28], showing high efficiency performance in a single-layer implementation. However, SIW dielectric losses — which account for the largest part of insertion losses — are very high for some loss-sensitive applications, such as the emerging millimeter wave systems [33]. Recently, the air-filled SIW (AFSIW) technology has been proposed [34], showing an insertion loss similar to metallic waveguides [33]. AFSIW geometry is based on multilayer PCB fabrication, where two top and bottom substrates enclose an inner substrate, which contains an air region. This three-layer implementation provides a higher Q-factor [30] and power handling than its dielectric-filled (DFSIW) counterpart [33].

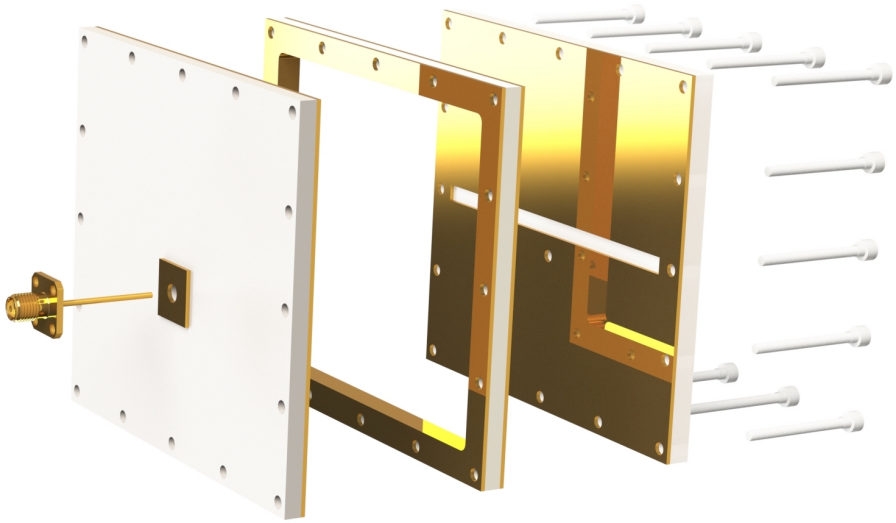

Figure 3.6: SIW implementation of the cavity-backed slot. Exploded view.

Inspired by [35], the CBSA is designed with AFSIW technology, implemented with a set of stacked laminates. An exploded view of this implementation is shown in Fig. 3.6[2]. Cavity sidewalls are obtained by milling a rectangular hole in one or more FR4 substrates. The milled sides are later metalized by round-edge plating. This technique allows combining different

[2]Substrate thicknesses in Fig. 3.6 are oversized for a better visualization.

substrate thicknesses to obtain the desired cavity height[3]. Two more layers are added to act as upper and lower cavity walls. One of these layers, referred as the top layer in this document, will contain the slot. On the bottom layer, the circuitry needed for an oscillator-antenna co-designed device will be integrated and, as such, the ground plane of this circuit will be the lower metallic wall of the cavity. To ensure that subsequent layers are galvanically connected and the substrates are properly aligned, layers are held together using a set of nylon screws around the edge of the cavity.

In order to generate the required electromagnetic field inside the cavity, SIW CBSAs can be fed with planar transmission lines, such as a microstrip line [36], coplanar waveguide (CPW) [37] and grounded coplanar waveguide (GCPW) [32]. However, these feeding techniques give rise to increased backside radiation and can suffer from disadvantageous dielectric and conductor losses [38]. To reduce backside radiation and losses, and increase power handling, a probe feeding mechanism is used, in which the feeding pin is the inner conductor of a coaxial line [39].

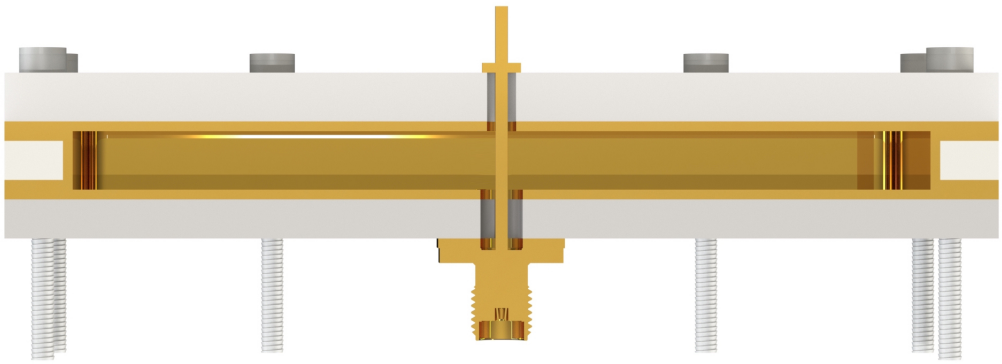

Figure 3.7: Cavity cut. Probe feeding technique representation in AFSIW cavity.

[3]In practice, an extra 70 $\mu$m from the copper on both sides of each FR4 layer will be added to the final height, although simulations show that the effects of this addition are insignificant.

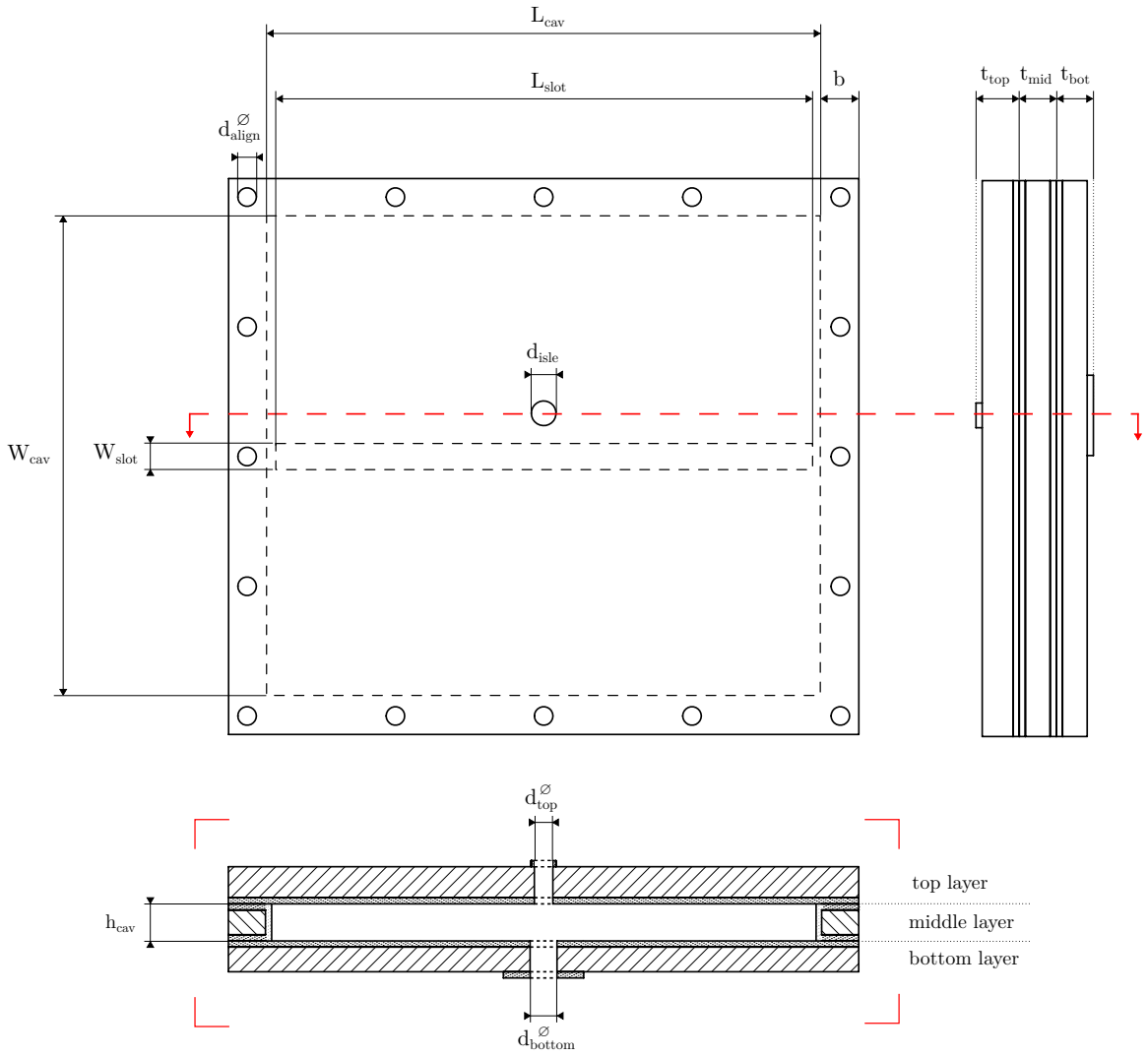


Figure 3.8: Coaxial-fed AFSIW cavity-backed slot antenna dimensions. Front, lateral and cross-sectional views.

A rendering of the probe feeding technique implemented in this design is shown in Fig. 3.7, where a commercially available coaxial connector with extended inner conductor is introduced into the cavity through a hole drilled in each of the top and bottom layers. The hole in the bottom layer is an air-filled continuation of the coaxial input. This way, the feeding network circuitry (i.e., the oscillator) is isolated from the radiating elements via a ground plane [39]. On the top layer, the hole is drilled with a diameter slightly larger than

the feeding pin, big enough for the probe to get through and still avoiding contact with the cavity top wall. A circular copper isle is used to solder the probe in the upper side of the top layer, thus being capacitively coupled with the cavity. This soldering isle adds a capacitive component to the input impedance, which effectively compensates the inductance normally associated with the probe [40].

A technical representation of the probe-fed AFSIW cavity-backed slot antenna designed for this dissertation is shown in Fig. 3.8, where the aforementioned feeding mechanism is depicted in the cross-sectional view. The holes drilled in the top and bottom layers have a diameter of $d_{top}$ and $d_{bottom}$, respectively; and the soldering isle diameter is denoted as $d_{isle}$. The component used for this feeding mechanism is a $50\,\Omega$ multicomp© female SMA (SubMiniature version A) connector. The connector's inner conductor has a $d_{pin} = 1.3\,\text{mm}$ diameter, so $d_{top}$ is set to 1.4 mm. The drilled hole in the bottom layer is set to $d_{bottom} = 4.35\,\text{mm}$, the same diameter as the teflon (formally, PTFE) insulation and outer conductor of the connector. The soldering isle has been set to $d_{isle} = 3\,\text{mm}$ after the optimization process to effectively match the device to the connector's $50\,\Omega$.

To implement the AFSIW cavity, two different types of commercial laminates are used. The middle layer is implemented in FR4 [41], a cheap and broadly available substrate, as this layer's purpose is to contain the air-filled region. In contrast, the top and bottom layers are implemented with low-loss Rogers© RO4350b [42]. These laminates have a dielectric constant of $\varepsilon_r = 3.66$ and a dissipation factor of $tan\delta = 0.0031$ at 2.45 GHz, which guarantee high performance of both slot and feeding circuitry. Top and bottom layers substrate thicknesses are $t_{top} = 250\,\mu\text{m}$ and $t_{bot} = 500\,\mu\text{m}$, respectively, to reduce losses and bandwidth widening [32]. The three substrates are eventually held together with a set of 16 ISO M3 nylon screws, so $d_{align}$ is set to 3 mm. To make room for the alignment screws, all layers are extended $b = 6\,\text{mm}$ around the cavity edges. Finally, a 1 mm-thick teflon piece cut off the coaxial connector insulation is placed inside the cavity attached around the probe, as a means of ensuring structural stability in the central part to prevent any cavity height alteration in the soldering process.

In order to obtain a resonance at 2.45 GHz of the fundamental mode $\text{TE}_{101}$, final cavity dimensions are $W_{cav} = 78\,\text{mm}$ and $L_{cav} = 90\,\text{mm}$. The resonant frequency of mode $\text{TE}_{101}$ can be obtained from (1), and is defined as:

$$f_{r_{101}} = \frac{1}{2\sqrt{\mu\varepsilon}}\sqrt{\left(\frac{1}{W_{cav}}\right)^2 + \left(\frac{1}{L_{cav}}\right)^2}. \tag{3.2}$$

Although the resonant frequency is independent from cavity height, this dimension is limited by commercially available substrate thicknesses. Therefore, to enable a three-layer AFSIW implementation, it has been fixed to $h_{cav} = 1\,\text{mm}$, a commercially available FR4 substrate thickness. However, despite not having an effect on mode resonance, cavity height has a direct relation with final bandwidth. A small cavity height promotes higher Q-factor — although not in a proportional way [43] — and hence: a narrow bandwidth.

The previously described AFSIW CBSA has been modeled and simulated in CST Microwave Studio. The electromagnetic field distribution, surface currents, radiation pattern and impedance performance have been thoroughly analyzed over a broad range of frequency points to understand the behavior of this cavity-backed slot antenna in particular, and to eventually obtain the optimized prototype that is presented in this section.

For the dimensions of the designed cavity, the resonant frequency of the $\text{TE}_{102}$ mode is 4.19 GHz. The surface currents of this mode get disrupted in the presence of the slot and tend to surround it to follow the path of least resistance. When the slot gets longer, this alteration of currents shift the resonant frequency of $\text{TE}_{102}$ to lower frequencies. For this design, where the slot fills the entire cavity length ($L_{slot} = 88\,\text{mm}$), the disruption is maximum, and $\text{TE}_{102}$ gets combined with $\text{TE}_{101}$ to obtain a hybrid mode field distribution around 2.45 GHz. In turn, slot width ($W_{slot} = 1.5\,\text{mm}$) does not have much influence on this disruption. For a fixed slot length, a greater slot width slightly decreases capacitance between the two long sides of the slot, having a low impact (smaller than slot length) on the hybrid mode impedance response and frequency allocation [32].

The modes operating in this cavity in a wide frequency range around 2.45 GHz are $\text{TE}_{101}$ and $\text{TE}_{102}$. At higher frequencies (around 5 GHz), the mode $\text{TE}_{301}$ gets excited and efficiently radiates ($\eta_{rad} > 70\%$) in an undesired two-lobe radiation pattern[4]. Below 4 GHz, when $\text{TE}_{301}$ influence is negligible[5], the required radiation pattern is stable in a broad range of frequencies. In the frequency range close to 2.45 GHz, modes $\text{TE}_{101}$ and $\text{TE}_{102}$ are combined differently.

[4]For a long slot with an excited $\text{TE}_{301}$ mode, electric field magnitude inside the slot completes a sinusoidal cycle. The radiation pattern is equivalent to a $2\lambda$-long dipole, in which electric current also completes a sinusoidal cycle [29].

[5]$\text{TE}_{301}$ resonant frequency for these cavity dimensions is 5.35 GHz (1).

Above 2.5 GHz, mode $TE_{101}$ is predominant, and radiation efficiency does not exceed 90%. Below 2.5 GHz, $TE_{102}$ is predominant, and the field distribution in each half of the cavity is out-of-phase, causing the slot to efficiently radiate ($\eta_{rad} > 90\%$). Exactly at 2.45 GHz, the electric field presents $135^{o}$ phase difference and strong magnitude contrast between both sides of the slot (Fig 3.9b) and radiation efficiency meets a local maximum. The electric field distribution inside the slot can be visualized in Fig. 3.9a, where electric field magnitude ($|E_z|$) presents one half-sinusoidal cycle.

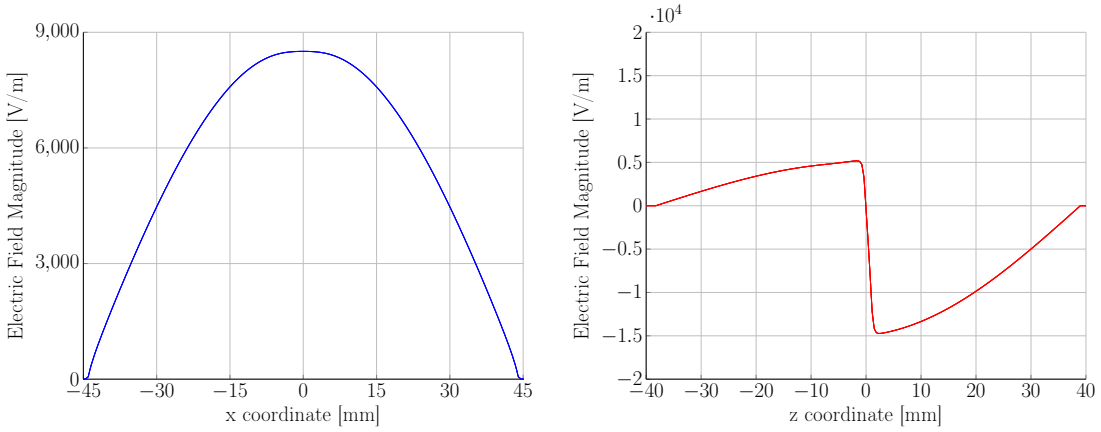


(a) Electric Field confined to the slot. Magnitude with respect to $\hat{x}$ ($z = 0$). ($|E_z|$ component)

(b) Hybrid mode Electric Field inside the cavity. Magnitude with respect to $\hat{z}$ ($x = 0$). ($|E_y|$ component)

Figure 3.9: Electric Field distribution in cavity and slot at 2.45 GHz.

The broadband evolution of the hybrid mode, in relation with the feeding mechanism, presents a set of resonances (low impedance) and antiresonances (high impedance) in the frequency range under consideration. At 2.45 GHz, the impedance response presents a resonance, which is part of a low-impedance region delimited by two antiresonances at lower and higher frequencies (Fig. 3.10). Therefore, matching at 2.45 GHz implies a high Quality Factor, as the surrounding high-impedance antiresonances directly constrain matching bandwidth.

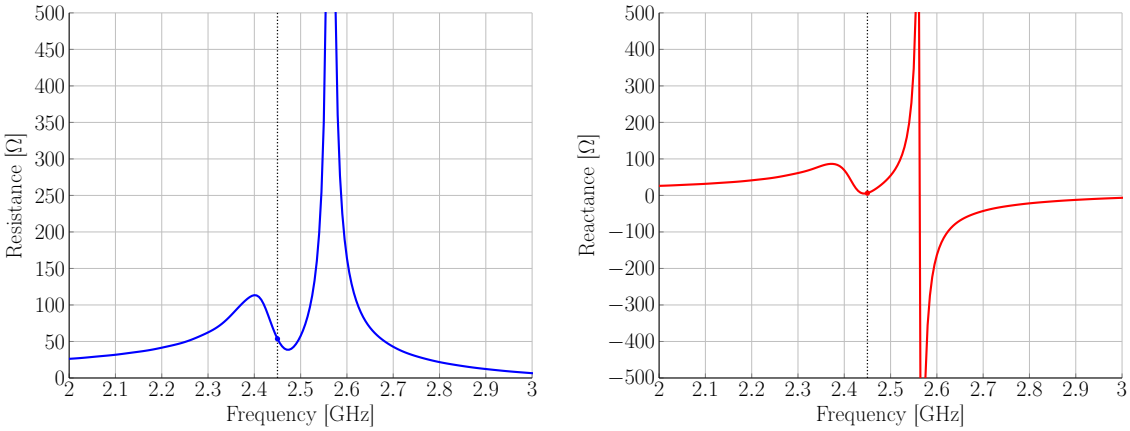


(a) Input Resistance

(b) Input Reactance

Figure 3.10: Simulated input impedance ($Z_{in}$).

The input impedance response seen from the coaxial port is shown in Fig. 3.10, where $Z_{in} = 53.58 + j6.33$ at 2.45 GHz. As previously stated, this frequency point is between two high-resistance regions, so matching conditions remain narrowband. The matched bandwidth can be visualized in the reflection coefficient ($|S_{11}|$), represented in Fig. 3.11. $|S_{11}| < -10$ dB is accomplished in a frequency region ranging from 2.42 GHz to 2.47 GHz, and within this 50 MHz bandwidth, matching to the input port is maximum at the central frequency 2.45 GHz, where $|S_{11}| = -23.3$ dB. Considering a Q-factor referred to the −10dB bandwidth, a Q = 49 is obtained.

Given the radiation pattern stability below 5 GHz and the radiation efficiency above design requirements in the region near 2.45 GHz (Fig. 3.12), the optimization process is mainly addressed to obtain optimum match at the operating frequency. The most significant changes to the impedance response are caused by the modification of the probe feed position. To achieve optimal matching to 50 Ω, the probe is located 5 mm from the center of the cavity in the $\hat{z}$ negative direction. To fine-tune the matching conditions into the final performance seen in Fig. 3.11, the $W_{slot}$ and $d_{isle}$ also play a role, even though their effect on the impedance is smaller.

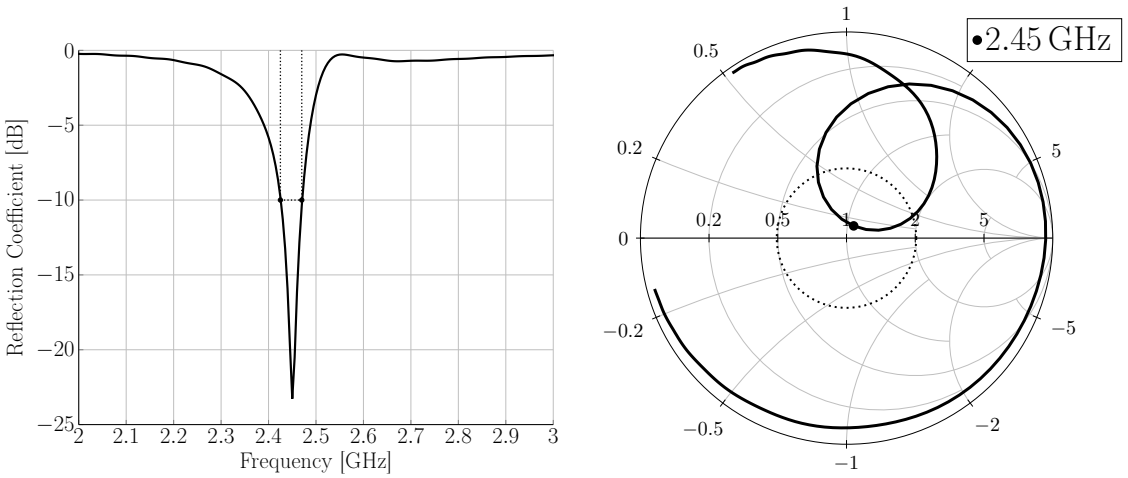


(a) Reflection Coefficient magnitude ($|S_{11}|$)

(b) Complex Reflection Coefficient ($S_{11}$). Smith Chart representation.

Figure 3.11: Simulated reflection coefficient ($S_{11}$)

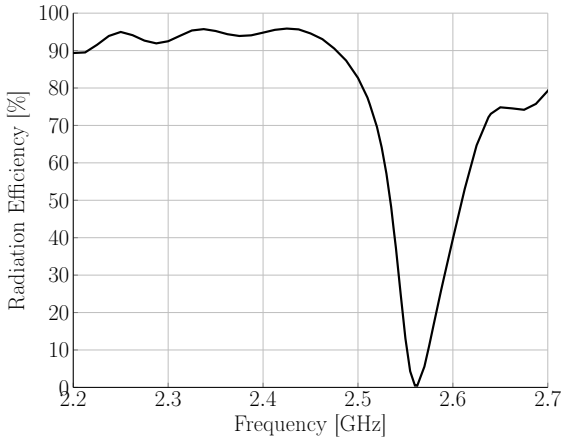


(a) Radiation Efficiency ($\eta_{rad}$)

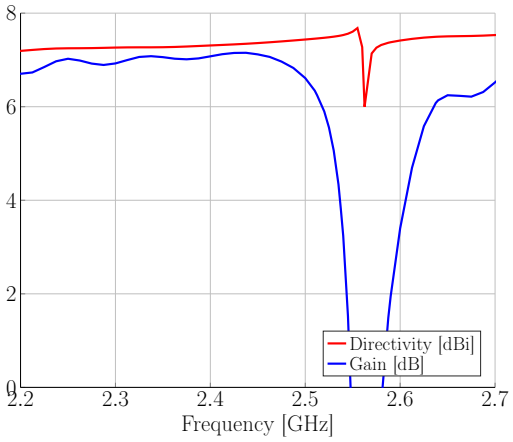


(b) Gain and Directivity

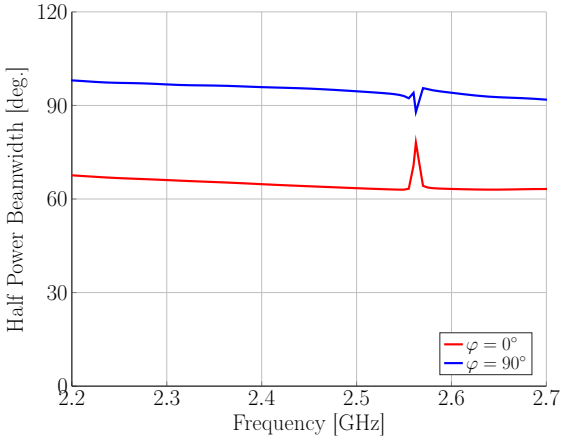


(c) Angular width (-3dB) of main lobe for plane E ($\varphi = 90°$) and H ($\varphi = 0°$)

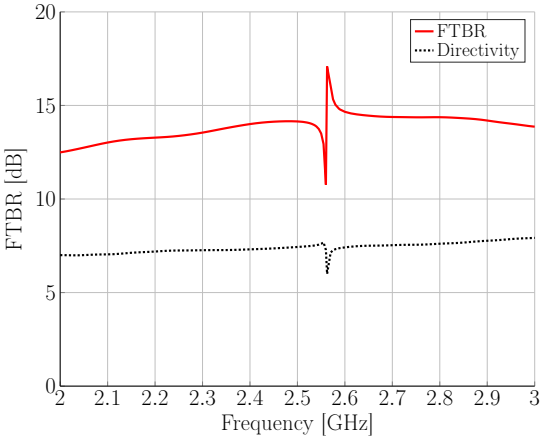


(d) Front-to-back ratio (FTBR) compared to Directivity

Figure 3.12: Radiation performance over frequency

Radiation pattern stability between 2.2 GHz and 2.7 GHz is reflected in Fig. 3.12. Radiation efficiency (Fig. 3.12a) exceeds 80% from 2.2 GHz to 2.5 GHz. Starting from 2.5 GHz the field distribution is dominated by a $TE_{101}$ mode, and specially at 2.55 GHz, $\eta_{rad}$ drops to 0% and the radiation pattern shape gets extremely perturbed. Overall, directivity and gain increase slightly over frequency (Fig. 3.12b), while the $-3$dB-referred angular width ($\Delta\theta_{-3dB}$) decreases (Fig. 3.12c). This evolution represents a tendency to a more directive lobe for higher frequencies, which is counterproductive to obtain a stable gain over a broad range of steering

angles for the antenna array. Furthermore, self-shielding of the CBSA topology from back-side radiation is shown in Fig. 3.12d. At 2.45 GHz (Fig. 3.13), as the FTBR is 14.1 dB for a directivity of D = 7.4 dBi. Due to the high efficiency ($\eta_{rad}$ = 95%), gain is 7.1 dB. The half-power beamwidth, which ranges from 64° in the H plane to 85° in the E plane, can be more intuitively visualized in Fig. 3.13 (dotted line), where $\varphi = 0°$ (H plane) and $\varphi = 90°$ (E plane) polar cuts of the three-dimensional radiation pattern are represented.

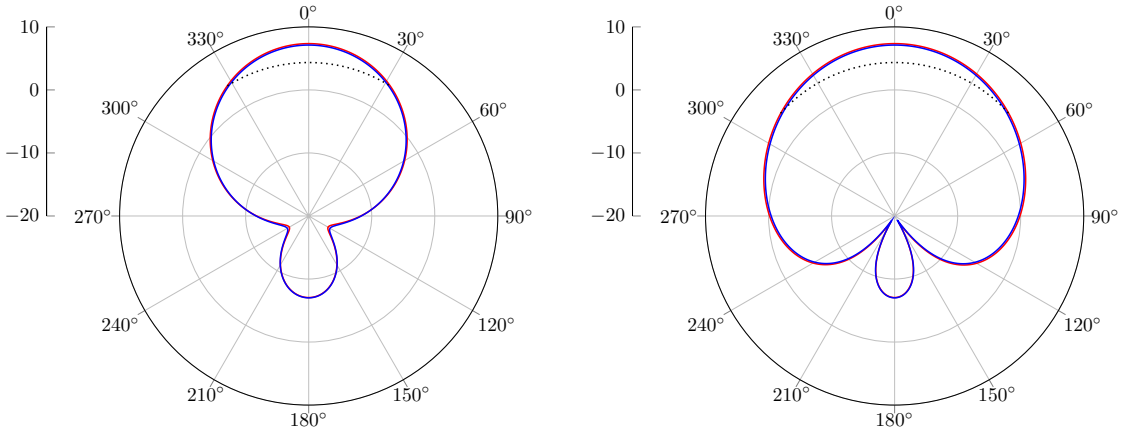


(a) $\varphi = 0°$ polar cut (H plane)

(b) $\varphi = 90°$ polar cut (E plane)

Figure 3.13: Directivity (red)[dBi] and Gain (blue)[dB] at 2.45 GHz

### Oscillator-ready CBSA Design

Simulation results previously shown represent the performance of a standalone cavity-backed slot antenna. However, in order to co-design an oscillator-antenna device, some considerations have to be taken into account. Without going into details about the oscillator design process, that will be described in the following Chapter, a few design decisions have been taken to obtain a co-designed antenna prototype for realistic results in the design of the active part of the device.

The probe feeding mechanism of the standalone antenna prototype is based on the use of a standard SMA commercial coaxial connector to conveniently validate simulation results with measurement equipment. Nevertheless, to integrate the oscillator onto the bottom layer the coaxial connector has been removed, and the probe — which remains unchanged — is fixed by means of a second soldering isle in the bottom layer. To connect this soldering isle

with the oscillator circuitry, a microstrip line sized for a 50 Ω characteristic impedance in the 500 $\mu$m-thick RO4350b substrate is employed.

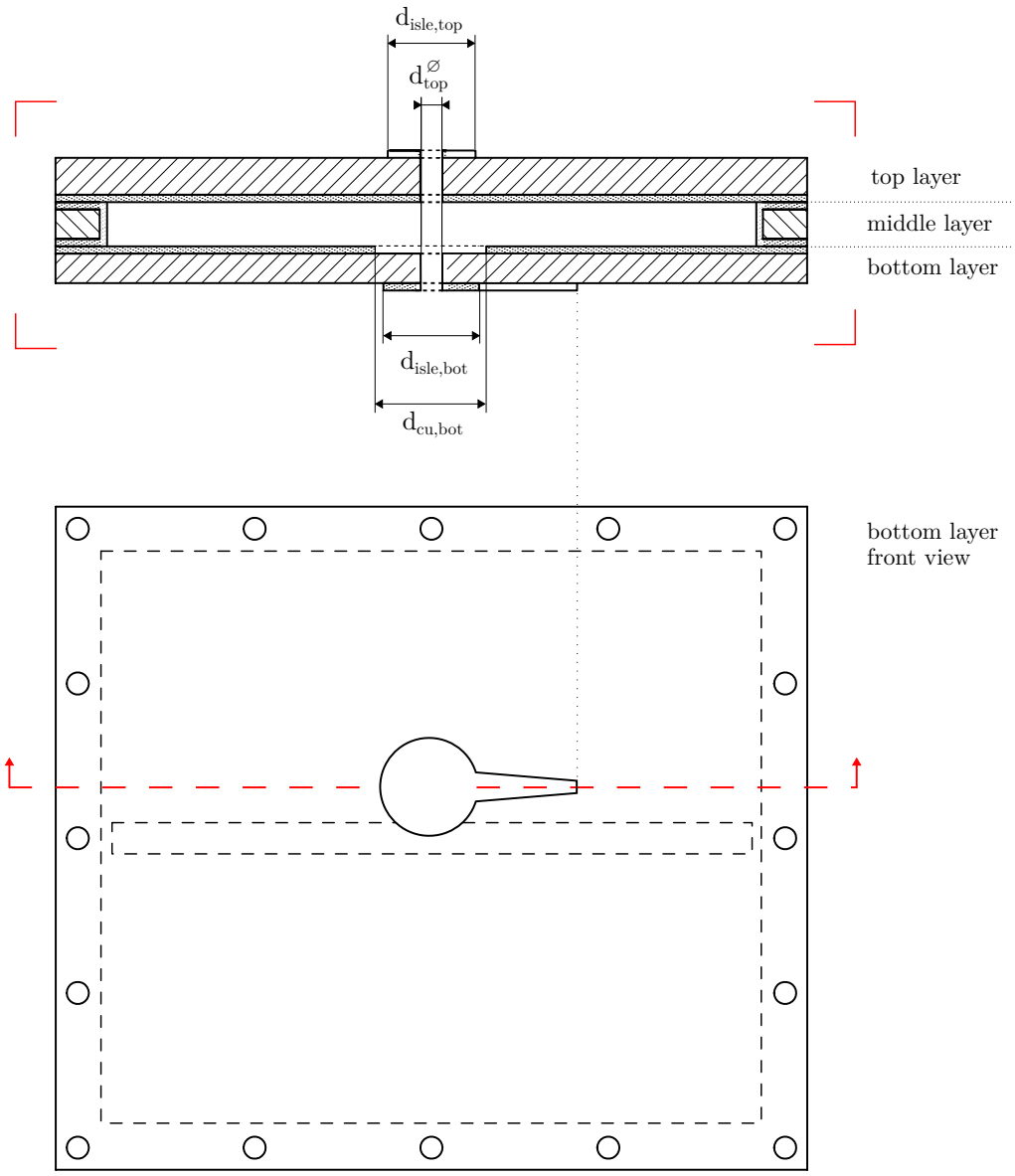


Figure 3.14: Microstrip-fed AFSIW cavity-backed slot antenna dimensions. Cross-Sectional and bottom layer front views.

The absence of the coaxial connector and the new feeding structure in the bottom layer provides additional variables to obtain an optimum match. The microstrip line, which has

been arbitrarily set to 10 mm long, has a tapered profile, as depicted in Fig. 3.14. In this case, the drilled hole in the top and bottom layers is the same ($d_{bottom} = d_{top} = 1.4\,\text{mm}$), and a $d_{cu,bot} = 4.22\,\text{mm}$ circle is removed from the copper layer of the bottom substrate that faces the interior of the cavity, in order to emulate a very thin coaxial input. Bottom layer's soldering isle has been optimized to a $d_{isle,bot} = 4\,\text{mm}$ diameter, while the isle on the top layer remains the same size ($d_{isle,top} = 3\,\text{mm}$).

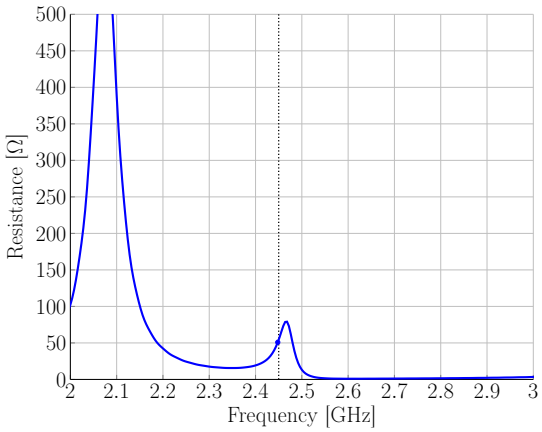


(a) Input Resistance

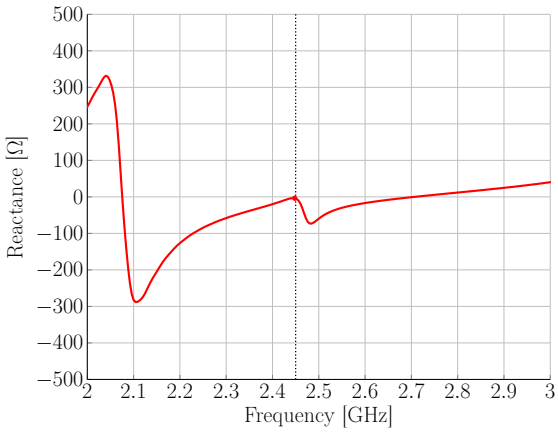


(b) Input Reactance

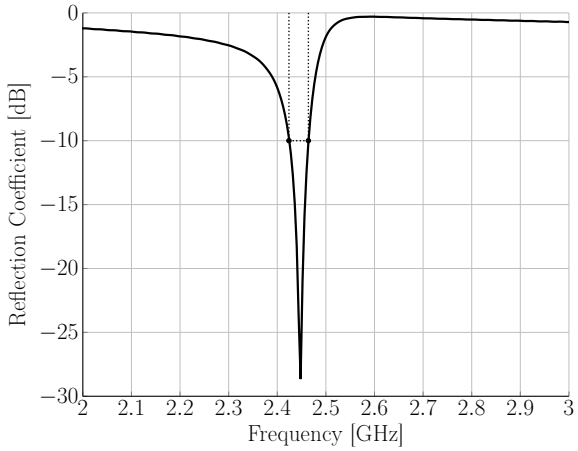


(c) Reflection Coefficient magnitude ($|S_{11}|$)

Figure 3.15: Simulated input impedance ($Z_{in}$) and reflection coefficient ($|S_{11}|$) of microstrip-fed co-designed antenna prototype.

Impedance response (Fig. 3.15) of the oscillator-ready antenna design presents substantial

changes in the magnitude of the two antiresonances that surround 2.45 GHz, but a low-impedance region remains around this frequency, so it remains possible to achieve a good match. Matching at the operating frequency, as shown in Fig. 3.15c, has moderately improved ($|S_{11}| = -28.7$ dB), while the Q-factor has increased to 61, due to a slightly narrow bandwdith (40 MHz) mainly caused by a matching point which lays on a resistance region steeper than in the standalone prototype. Radiation performance remains stable, with a small radiation efficiency reduction ($\eta_{rad} = 89\%$). A higher Front-to-Back Ratio (FTBR = 20.5 dB) shows a fourfold reduction of backside radiation power with respect to the standalone antenna. As a result, co-designed CBSA's overall performance complies better with the antenna system requirements embraced in Section 3.1.

The final performance at the central operating frequency (2.45 GHz) of the standalone and co-designed CBSA simulated prototypes is quantitatively summarized in the following table.

| **Prototype** | | **Standalone** | | **Co-designed** | |
|---|---|---|---|---|---|
| Input Resistance | $R_{in}$ | 53.6 | Ω | 50.9 | Ω |
| Input Reactance | $X_{in}$ | 6.3 | Ω | −3.6 | Ω |
| Reflection Coefficient | $\|S_{11}\|$ | −23.3 | dB | −28.7 | dB |
| Matched Bandwidth | BW | 50 | MHz | 40 | MHz |
| Quality Factor | Q | 49 | | 61 | |
| Directivity | D | 7.4 | dB | 7.3 | dB |
| Radiation Efficiency | $\eta_{rad}$ | 95 | % | 89 | % |
| Gain | G | 7.1 | dB | 6.8 | dB |
| Angular width (E) | $\Delta\theta^{E}_{-3\text{dB}}$ | 85 | deg. | 96 | deg. |
| Angular width (H) | $\Delta\theta^{H}_{-3\text{dB}}$ | 64 | deg. | 67 | deg. |
| Front-to-Back Ratio | FTBR | 14.1 | dB | 20.5 | dB |

Table 3.1: Antenna prototype simulation results

# Chapter 4

# Oscillator Design

This chapter will cover the design process of the oscillator, from design requirements to final working prototype, starting with Section 3.1, where the oscillator specifications are described. The chosen topology and the operating principle are explained in Section 3.2 and Section 3.3, respectively. To conclude, Section 3.4 describes the design process, includes key simulation results and gives the final oscillator layout.

## 4.1 Design Requirements

As part of the co-designed oscillator-antenna device, this module is designed to oscillate at 2.45 GHz. To prevent interference with co-existing technologies in the same band, the European Telecommunications Standards Institute (ETSI) sets a maximum[1] Equivalent Isotropic Radiated Power (EIRP[2]) of 36 dBm for the 2.45 GHz ISM band [44, 45]. Considering the gain of the simulated co-designed antenna is 6.8 dB, the output power of the oscillator ($P_{osc}$) should be limited to 29.2 dBm ($\sim 1$ W).

Taking into account that the oscillator will be an element of a coupled oscillator array, and that an external signal will be injected into it, some precautions should be taken for correct operation of the injection locking principle. Locking range dependency on the oscillator's

[1] Depending on the modulation scheme of the transmission system maximum EIRP values may vary [44].

[2] EIRP is a standardized definition of the hypothetical output power that an isotropic antenna would have to radiate to equate the signal strength that the actual source is radiating in the main lobe direction. It is defined by the power input to the antenna multiplied by its gain.

Q-factor and signal amplitude was mentioned in Chapter 2, and it is defined by:

$$\Delta w_L = \frac{w_{osc}}{2Q} \cdot \frac{\mathrm{A}_{inj}}{\mathrm{A}_{osc}}, \tag{4.1}$$

assuming $\mathrm{A}_{osc} \ll \mathrm{A}_{inj}$, where $\mathrm{A}_{inj}$ and $\mathrm{A}_{osc}$ represent the injected and output signal amplitudes, respectively [6].

To ensure that the locking range ($\pm\Delta w_L$) will not exceed the co-designed antenna matched bandwidth ($2.45\,\mathrm{GHz} \pm 20\,\mathrm{MHz}$), the Q-factor has to be larger than $61.25\,\mathrm{A}_{inj}/\mathrm{A}_{osc}$ to enable optimum match throughout the full range of phase shift between elements [5]. Obviously, the injected signal amplitude and frequency-tunable range can be decided *a posteriori* to fulfill this requirement, but a high Q-factor will decrease the external oscillator's necessary output power and, as a result, power consumption of the whole system will be reduced. Either way, the oscillator should be designed under the assumption that the $\mathrm{P}_{osc}$ is larger than $\mathrm{P}_{inj}$ to ensure the injected power can be successively coupled into adjacent oscillators.

Regarding the oscillator output signal, the optimized design should aim for harmonic purity. To obtain a sinusoidal time-domain waveform at the operating frequency, harmonic suppression should preferably exceed 20 dB. Additionally, the oscillation needs to achieve time-domain steady-state. Avoiding potential non-harmonic oscillations in a broad range of frequencies is also preferred to prevent causing interference to out-of-band technologies.

Finally, to ensure seamless integration with the co-designed antenna, the circuit layout has to be implemented in the bottom layer of the previously designed AFSIW cavity. The co-designed oscillator design process needs to take into account antenna impedance response and, therefore, its integration cannot imply the modification of any of the AFSIW CBSA dimensions that directly affect the antenna's overall performance. Should there be any necessary modification to the AFSIW structure, the changes would need to be reflected accordingly in the antenna simulations.

## 4.2 Oscillator Topology

Oscillators use nonlinear active devices to convert DC to a sinusoidal RF signal. At low frequencies, a steady-state solution is often obtained using a transistor-based amplifier with a frequency-dependent external feedback [30]. Well-known topologies, such as Hartley, Colpitts

and Clapp [46] oscillator circuits can be represented by this operation mode. However, at microwave frequencies higher than 500 MHz, the conceptualized assumption that both amplifier and external feedback act independently is no longer valid, given the increasing parasitic effects and coupling between components. As a result, guaranteeing oscillation conditions can become unwieldy.

A different approach is used to design oscillators at high microwave frequencies. Negative resistance oscillators represent a design technique where transistors are biased to a negative resistance operating point, thus leading to a different circuit topology than their low-frequency counterparts.

A first step in this design procedure is designing a functioning amplifier, which will later be destabilized to obtain an oscillating output. Among the possible amplifier types, common-emitter and common-base are the frequently chosen topologies. To obtain an unstable operating point, internal positive feedback is added to the amplifier circuit, and to simplify this process, a common-base amplifier is designed for this module, as the RF signal inside this type of amplifiers is always in-phase [47].

## 4.3 Operation Principle

As previously mentioned, a negative resistance oscillator is designed using a destabilized amplifier. Making use of traditional amplifier stability analysis, this amplifier is properly loaded to sustain a frequency-dependent steady-state oscillation.

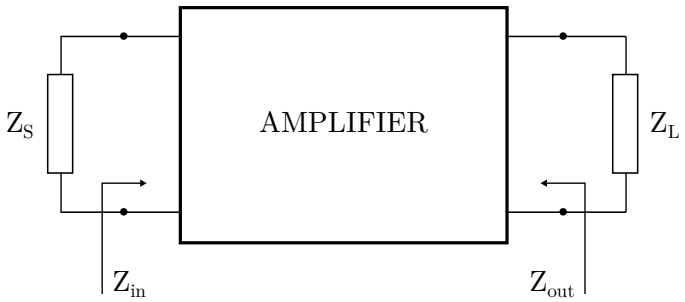


Figure 4.1: Two-port diagram of a conventional amplifier.

The two-port diagram shown in Fig. 4.1 represents an amplifier terminated with certain source ($Z_S$) and load ($Z_L$) impedances. The impedance seen from the input ($Z_{in}$) and the

output ($Z_{out}$) depend on load and source impedances, respectively. From stability theory, it is known that for a given transistor biasing, there are a number of termination impedances that cause either $R_{in} < 0$ or $R_{out} < 0$, which are often represented with stability circles in the Smith chart.

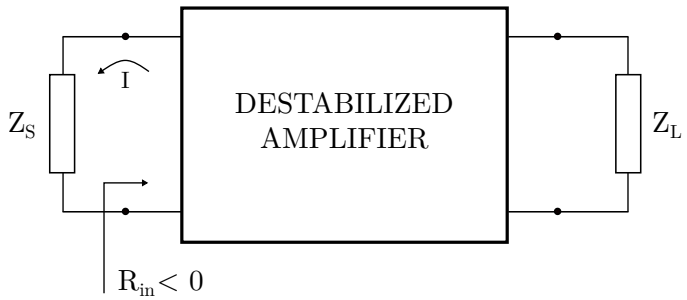


Figure 4.2: Two-port diagram of a destabilized amplifier. Negative resistance seen at the input port.

Since the voltages at both amplifier ports are related, oscillation will occur all over the circuit regardless of the destabilized port. To particularize, a $Z_L$ inside the unstable region of the output stability circle can be considered, leading to a negative input resistance (Fig. 4.2). While a positive resistance represents energy dissipation, a negative resistance implies loss compensation. If the energy dissipation at the input port is smaller that the incident energy from the amplifier, any excitation, noise or small perturbation in the circuit will be repeatedly amplified as time progresses and an oscillation will build up. Oscillation start-up conditions can be expressed as:

$$R_S + R_{in} < 0 \tag{4.2a}$$

$$X_S + X_{in} = 0 \tag{4.2b}$$

The oscillation is critically dependent on the nonlinear behavior of $Z_{in}$. The impedance seen from the input port of the amplifier depends heavily on the amplitude of the signal being amplified. As signal strength is increased to large-signal conditions, the resistive part magnitude of $Z_{in}$ decreases, i.e., $R_{in}$ becomes less negative, while the reactive part remains relatively constant [46]. When $|R_{in}|$ is the same value as $R_S$, the amplifier is effectively compensating the losses of the passive source without generating additional energy, that is,

the oscillation is showing a constant envelope. Therefore, the conditions for a steady-state oscillation can be expressed as:

$$R_S + R_{in} = 0 \tag{4.3a}$$

$$X_S + X_{in} = 0 \tag{4.3b}$$

Equations (4.2b) and (4.3b) imply that the source and amplifier reactances are conjugate matched, which means there is a strong frequency dependence. Ideally, these conditions must be met at exactly one frequency — the frequency of oscillation ($w_{osc}$) — and at a specific signal level.

## 4.4 Co-designed Oscillator Prototype

The process to design an oscillator prototype is based on the steps followed in [5, 48], where a negative resistance oscillator circuit is effectively synthesized with a step-by-step approach. The working prototype described in this section was designed using the following procedure:

1. Amplifier design
2. Amplifier destabilization
3. Output matching network design
4. Determination of source impedance to ensure oscillator start-up
5. Time and frequency-domain simulations

The design of the following schematics was performed with Keysight's ADS.

### Amplifier design

To design the amplifier, a common-base topology has been used. As it was briefly justified in Section 4.2, common-base amplifier topologies, unlike common-emitter, present in-phase input and output signals. This feature simplifies and reduces the necessary components for

amplifier destabilization. The active component used for this amplifier is a NPN BJT, which has superior phase noise performance to MESFETs [46]. The selected model is a BFP193 transistor [49], from Infineon Technologies, ideal for low-noise and high-gain amplifiers, which has a transition frequency ($f_T$) of 8 GHz. The $f_T$, sets the frequency at which the gain of the transistor drops to unity, and therefore, the maximum frequency at which the oscillation can build-up. This way, $f_T$ is sufficiently high to oscillate at 2.45 GHz while ensuring high-frequency oscillations will be minimized [46].

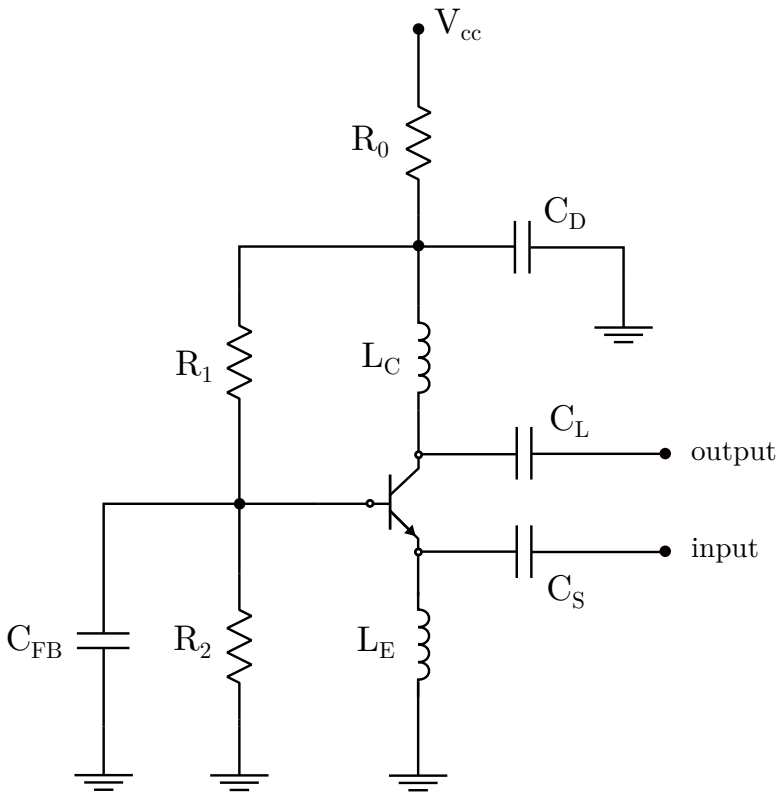


Figure 4.3: Schematic of a common-base amplifier.

The common-base amplifier schematic is shown in Fig. 4.3, the values of the ideal components are specified in Table 4.1 and the simulated DC operating point is shown in Table 4.2. The transistor is biased to $V_{CE} = 2.03\,\text{V}$, well below the collector-emitter breakdown voltage (12 V), obtained with $R_0$, which drops some of the power supply voltage ($V_{cc} = 3.3\,\text{V}$). $R_1$ and $R_2$ act as a voltage divider, setting the voltage at the base ($V_B = 832\,\text{mV}$). A very small

current flows into the base ($I_B = 270\,\mu\text{A}$), which make $I_E \simeq I_C = 20.8\,\text{mA}$, as common-base topologies do not amplify current.

Two ideal DC block capacitors are placed at the RF input (emitter) and output (collector). Another capacitor ($C_{FB}$) is attached to the base in order to connect this terminal to ground at RF frequencies. Additionally, two inductors are connected to the collector ($L_C$) and to the emitter ($L_E$), which act as RF chokes. $L_E$, however, also adds inductive degeneration to the emitter, as a means of ensuring the operating point is stable against any change of temperature.

| | | |
|---|---|---|
| $R_0$ | 51 | Ω |
| $R_1$ | 300 | Ω |
| $R_2$ | 200 | Ω |
| $C_{FB}$ | ideal RF bypass | |
| $C_D$ | ideal RF bypass | |
| $C_L$ | ideal DC block | |
| $C_S$ | ideal DC block | |
| $L_C$ | ideal DC Feed | |
| $L_E$ | ideal DC Feed | |

Table 4.1: Component values of common-base amplifier.

| | | |
|---|---|---|
| $V_{cc}$ | 3.3 | V |
| $I_{cc}$ | 24.5 | mA |
| $P_{DC}$ | 19 | dBm |
| $V_{CE}$ | 2.03 | V |
| $V_{BE}$ | 811 | mV |
| $I_B$ | 270 | $\mu$A |
| $I_C$ | 20.8 | mA |
| $I_E$ | 20.8 | mA |

Table 4.2: DC Operating Point of common-base amplifier.

### Amplifier destabilization

The RF bypass capacitor at the base has a high impedance for low frequencies and low impedance for higher frequencies. Adding a series inductance to this capacitor creates a tunable resonance, which will act as a low impedance path to ground for a certain range of frequencies. That is, adding an inductor ($L_{FB}$) in series with $C_{FB}$ creates an internal positive feedback in a band around the LC resonance. A new schematic is shown in Fig. 4.4, where this additional component is reflected.

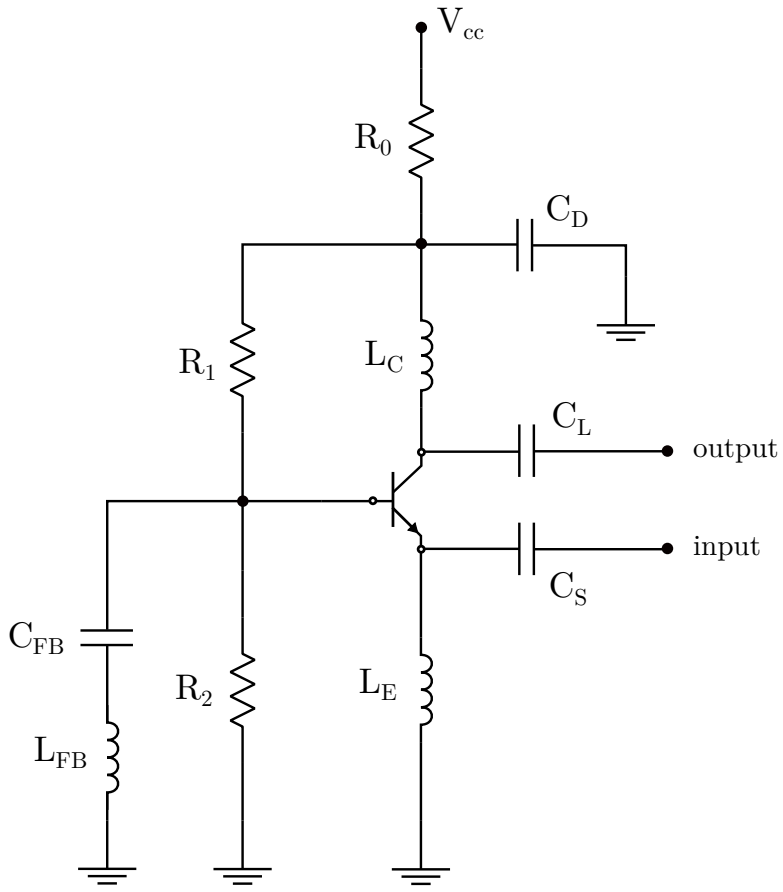


Figure 4.4: Schematic of a common-base amplifier with positive feedback at the base.

The values of the components of this series LC branch are shown in Table 4.3, and they resonate at 2.37 GHz. However, according to Fig. 4.5, the potentially unstable region peaks at the operating frequency, 2.45 GHz. This is due to the fact that the transistor's parasitic capacitances (such as $C_{BC}$) also contribute to the resonance.

| | | |
|---|---|---|
| $R_0$ | 51 | Ω |
| $R_1$ | 300 | Ω |
| $R_2$ | 200 | Ω |
| $C_{FB}$ | 1.5 | pF |
| $C_D$ | ideal RF bypass | |
| $C_L$ | ideal DC block | |
| $C_S$ | ideal DC block | |
| $L_{FB}$ | 3 | nH |
| $L_C$ | ideal DC Feed | |
| $L_E$ | ideal DC Feed | |

Table 4.3: Component values of destabilized common-base amplifier.

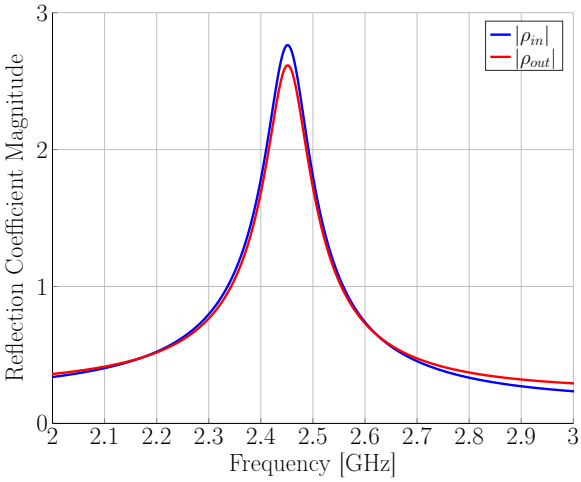


Figure 4.5: Port reflection coefficients ($|\rho_{in}|$, $|\rho_{out}|$) in the destabilized amplifier.

At this moment, when standard port terminations ($Z_L = Z_S = 50\,\Omega$) are being used in the simulations, $R_{in}$ and $R_{out}$ present negative value. The unstability of this circuit can be clearly visualized in Fig. 4.5, as $|\rho_{in}|$ and $|\rho_{out}|$ show magnitudes above 1 in a broad range of frequencies around 2.45 GHz.

Nevertheless, if a different load impedance is used, the unstability can be maximized. A Smith chart representation of the output stability circle is shown in Fig. 4.6. The positive feedback causes the $|\rho_{in}| = 1$ circumference (**black**) to almost fill the entire chart. This way, virtually any $Z_L$ would produce a negative value at the input ($|\rho_{in}| > 1$). Additional circles have been drawn to observe the possible values of $Z_L$ that increase $|\rho_{in}|$.

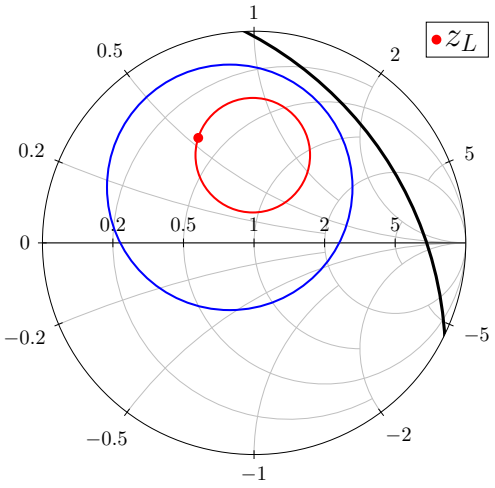


Figure 4.6: Smith chart representation of constant $|\rho_{in}|$ circles: $|\rho_{in}| = 1$ (**black**), $|\rho_{in}| = 2$ (**blue**) and $|\rho_{in}| = 3$ (**red**).

### Output matching network design

Among the infinite possibilities of $Z_L$, a value that increases the magnitude of $|R_{in}|$ which, at the same time, stays deep inside the stability circle will protect the unstability from deviations in the component values and guarantee good start-up conditions. The load impedance selected to increase the unstability is $Z_L = 18.6 + j26.9\,\Omega$, which belongs to the $|\rho_{in}| = 3$ circumference (Fig. 4.6 — **red**).

The matching network designed for the output port is shown in Fig 4.7, which consists of a series capacitor, followed by a transmission line and a shunt stub. The lines, which are ideal simulation models, are configured for a characteristic impedance ($Z_o$) of $50\,\Omega$ at 2.45 GHz. The capacitor ($C_S$) is the previously ideal DC block, which now participates to match the load.

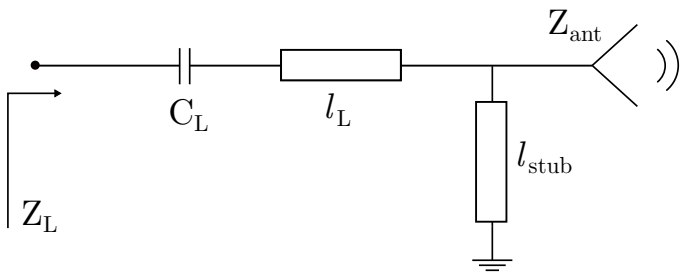


Figure 4.7: Output matching network to achieve the selected $Z_L$.

| $Z_{ant}$ | **Single Value** | | **CST Model** | |
|---|---|---|---|---|
| $C_S$ | 10 | pF | 10 | pF |
| $l_L$ | 11.23 | deg. | 33.7 | deg. |
| $l_{stub}$ | 13.95 | deg. | 31.95 | deg. |

Table 4.4: Component values of the output matching network.

As a first step to synthesize this matching network, it has been designed to match the impedance of the antenna at the operating frequency, $Z_{ant}\,(2.45\,\text{GHz}) = 50.9 - j3.6$ (Table 3.1). Afterwards, the impedance results from the co-designed AFSIW CBSA have been exported from CST and added as $Z_{ant}$ of the schematic. The change from $Z_{ant}\,(2.45\,\text{GHz})$ to a frequency-dependent $Z_{ant}$ slightly affects the length of $l_L$ and $l_{stub}$ (Table 4.4).

### Determination of source impedance

The complex input reflection coefficient for the chosen $Z_L$ is $\rho_{in} = 3.04\angle{-21.3}°$ which, referred to $50\,\Omega$, represents an input impedance of $Z_{in} = -90 + j24\,\Omega$. According to the aforementioned start-up conditions (4.2), the source impedance should compensate the conjugated reactance and some resistance. To determine the amount of resistance that the source will have, a widespread rule of thumb is making $R_S$ one-half to one-third of the small signal value of $|R_{in}|$ [46]. This way, the amplifier input resistance will be sufficiently more negative than the source, so that oscillations can grow. As a result, the source impedance is set to $Z_S = 30 + j24\,\Omega$, which is accomplished with an RC series circuit, composed of a $30\,\Omega$ resistor and a 2.7 pF DC block capacitor. The final ideal schematic is shown in Fig. 2.8.

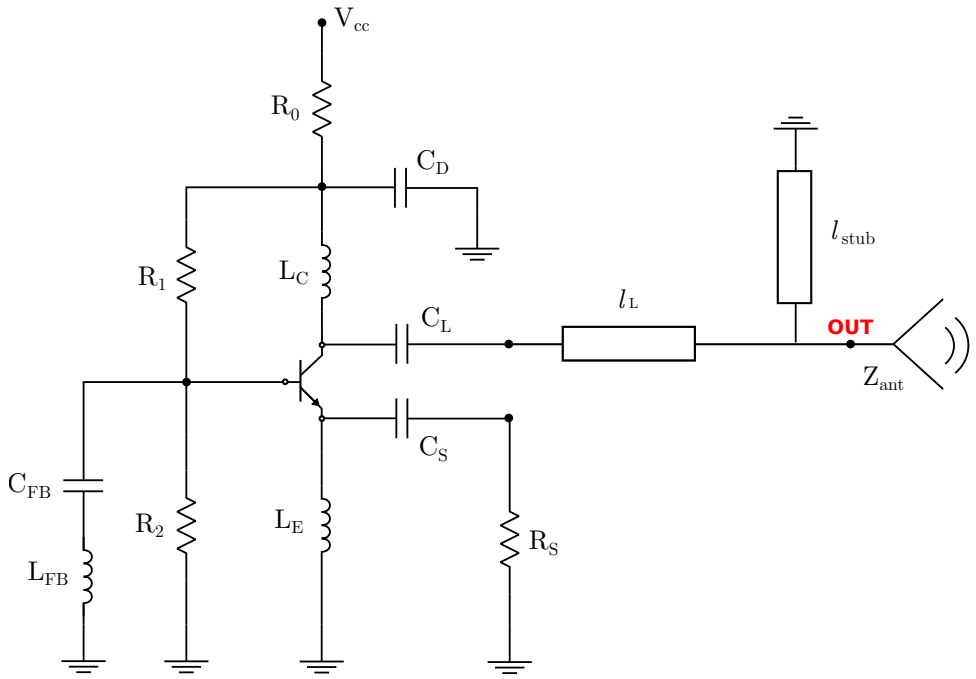


Figure 4.8: Ideal schematic of the oscillator.

### Time and frequency-domain simulations

As mentioned before, the oscillator's steady-state regime happens for large-signal conditions, when the nonlinearities of the amplifier reduce the magnitude of $R_{in}$. Therefore, some simulations need to be done to validate the behavior of the oscillator with large-signal magnitudes.

Fig. 4.9 encompasses the performance of the ideal oscillator in both time and trequency-domain. Using the imported AFSIW CBSA impedance response as an output port in the simulation provides the $|\rho_{out}|$ response shown in Fig. 4.9a. A narrowband and large unstability is clearly visualized at 2.45 GHz in small-signal range.

To represent the time domain response of the oscillator, a transient simulation has been configured at the **OUT** node (Fig. 4.8). Fig. 4.9b shows the sinusoidal shape of the time-domain waveform at this node, whereas Fig. 4.9c shows the evolution over time from small-signal to large-signal steady state. A way to reliably determine if the device is oscillating at the expected frequency is calculating the Fast Fourier Transform (FFT) of a sufficiently

long waveform. In Fig. 4.9e, a broadband FFT of the steady-state part of the waveform is represented, which peaks at 2.48 GHz.

Finally, to double-check the oscillating frequency simulation, and to determine the expected output power at the node, a Harmonic Balance (HB) simulation is configured. In ADS, there is an option to assist the HB with the results from transient to operate more efficiently (Transient Assisted Harmonic Balance). Transient simulator detects steady-state 53 ns after starting, and communicates relevant information with HB, leading to the results shown in Fig. 4.9f. HB predicts a 8.5 dBm oscillation at the **OUT** node, with 25 dB of second harmonic suppression, at the same frequency as the transient simulation, therefore validating these results for both time and frequency domains.

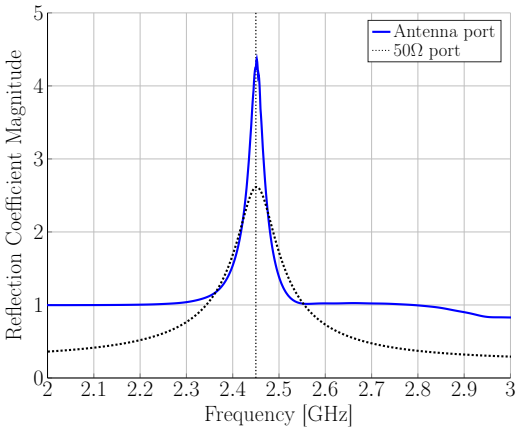


(a) $|\rho_{out}|$ with antenna port compared to standard 50 Ω port

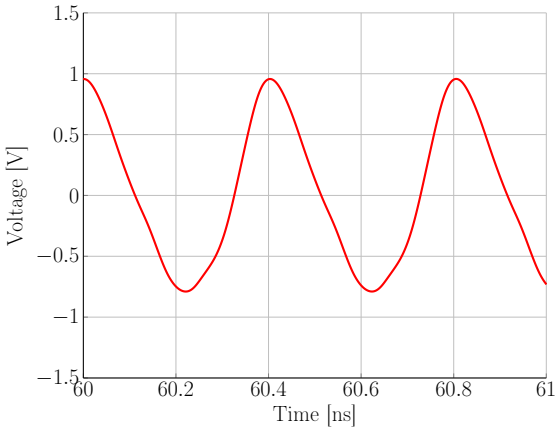


(b) Output waveform in steady-state regime

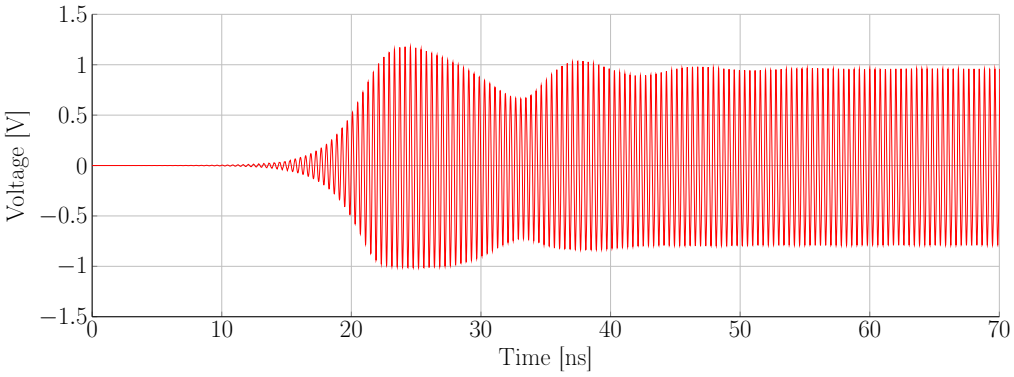


(c) Oscillation start-up

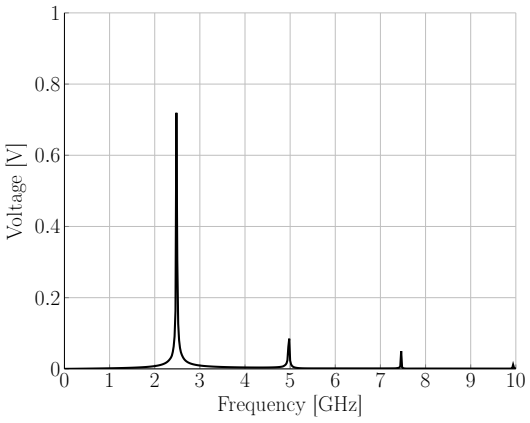


(d) FFT of time-domain output waveform

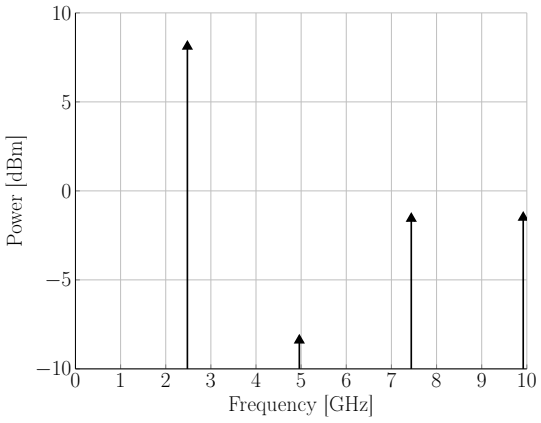


(e) HB simulation

Figure 4.9: Performance of the oscillator with ideal components.

### Layout-friendly prototype

The last step in the process is designing a schematic to eventually manufacture an oscillator prototype. The main purpose of this part is changing all the ideal component models to realistic models provided by the manufacturers. The transmission lines, which were also ideal, are modelled properly considering the substrate the circuit is going to be implemented on and additional transmission lines and T-junctions are included in the circuit in order to seamlessly connect all components in a layout-friendly schematic. This, of course, changes the response of the oscillator. Therefore, to prevent any degradation of power and harmonic purity, and to ensure the oscillating frequency stays close to 2.45 GHz, it is important to know the effects every component has on the final performance. The designed layout-friendly schematic with realistic components, referred as *real schematic* in this document, is illustrated in Fig. 4.10.

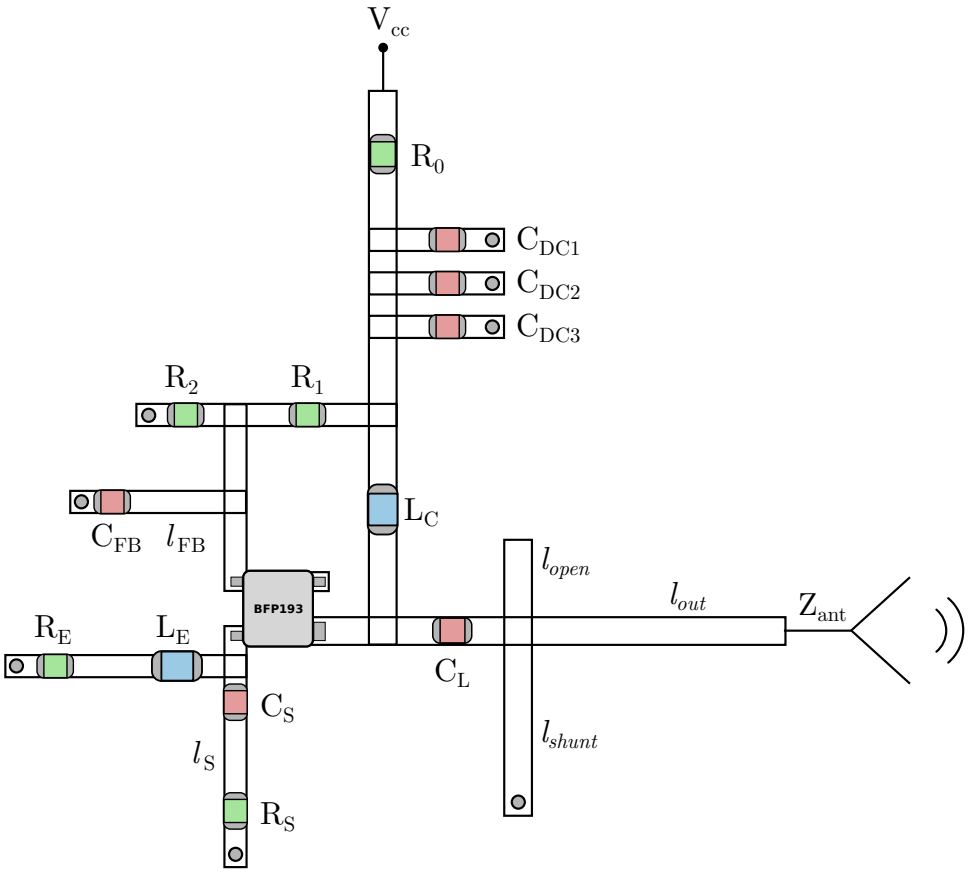


Figure 4.10: Real schematic of the oscillator.

The bottom layer of the AFSIW CBSA, on which the oscillator will be integrated, is a Rogers© RO4350b [42] with a thickness of $t_{bot} = 500\,\mu$m. At 2.45 GHz, a transmission line with a characteristic impedance of $Z_{co} = 50\,\Omega$ has a width of $W_{50} = 1.07\,$mm on this substrate, which is the same width of the microstrip line in the microstrip-fed CBSA model simulated in CST (Fig. 3.14). The output matching network, which is directly connected with the antenna model ($Z_{ant}$), is based on $W_{50}$ microstrip lines.

The BFP193 transistor's footprint has two diagonally opposite emitter pads, which have been connected with a thin transmission line underneath the component. Additional transmission lines have been used to distribute the components in the layout. Unfortunately, some of these lines drastically change the response of the entire circuit. The output matching network, in particular, turns out to be most sensitive to these changes and now features an open

stub for additional tuning ability.

To allow fine-tuning of the destabilizing internal feedback, the inductor $L_{FB}$ is implemented in a distributed form ($l_{FB}$). A similar approach has been followed in the source impedance, where the RC circuit is separated with a transmission line ($l_S$). These two lines ($l_{FB}$ and $l_S$) are key to fine-tune the frequency of oscillation, as the feedback controls the unstable range of frequencies and the source impedance controls the net reactance.

The RF chokes at the collector and emitter are now modelled with two 62 nH inductors, optimized for high impedance at the operating frequency. The inductor at the emitter was also used to generate internal negative feedback to stabilize the DC operating point. To control the amount of feedback, a resistor $R_E$ has been connected to this inductor. The dissipation that $R_E$ causes can be used to reduce the power of the overtones when harmonics increase, thus being important to guarantee harmonic purity.

To predict the oscillating frequency, an additional simulation has been configured. ADS' component *OscTest* can be placed in the feedback branch of the oscillator to gather information useful to guarantee oscillation start-up. The results, shown in Fig. 4.11, are the gain and phase over frequency at a node placed in the feedback branch. The oscillation will start-up and achieve steady-state if the gain exceeds unity and the phase crosses zero (from positive to negative values), which matches the necessary conditions for oscillation according to the Barkhausen criterion [5]. This conditions, although not sufficient to guarantee oscillation, are the basis of external feedback oscillators, and can be cautiously used as a means to predict the performance of this oscillator in a short simulation time.

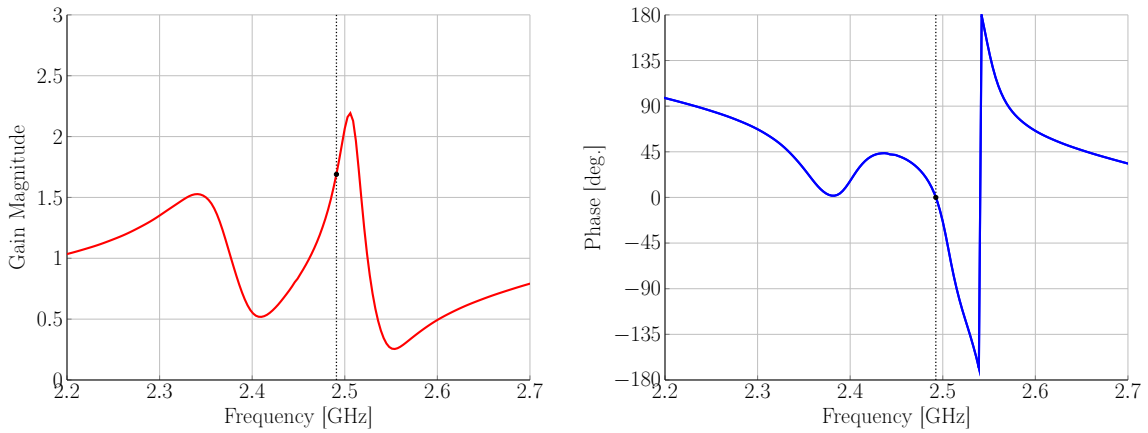


(a) Loop Gain (b) Phase

Figure 4.11: OscTest gain and phase response

The gain and phase for the optimized real schematic are represented in Fig 4.11. The shape of the curves is mainly caused by the steepness of the CBSA impedance. Then, these curves can be effectively warped — although not in a predictable way — by changing the output matching network components. Tuning the output matching network is key to prevent oscillation conditions to be met in any other frequency. Empirically, it has been observed that the oscillation frequency matches the one predicted by this simulation if the phase crosses zero with high negative slope, as shown in the graph (Fig 4.11), where the conditions are satisfied at 2.48 GHz. To fine-tune the frequency, $l_{FB}$ is the most effective component up to a certain degree, when the negative phase slope decreases and the results stop being reliable. Once the graph has been optimized, $R_S$ can be used to adjust the gain with no effect on the shape of the curve and a direct relation with the output power.

The real oscillator performance is shown in Fig. 4.12. Using a port referred to the impedance of the co-designed CBSA, the output reflection coefficient is plotted in Fig 4.12a, which shows a high degree of unstability in the circuit at 2.49 GHz.

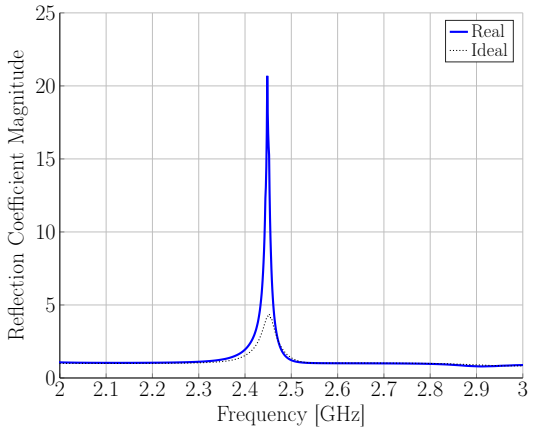


(a) $|\rho_{out}|$ with antenna port compared to the ideal schematic

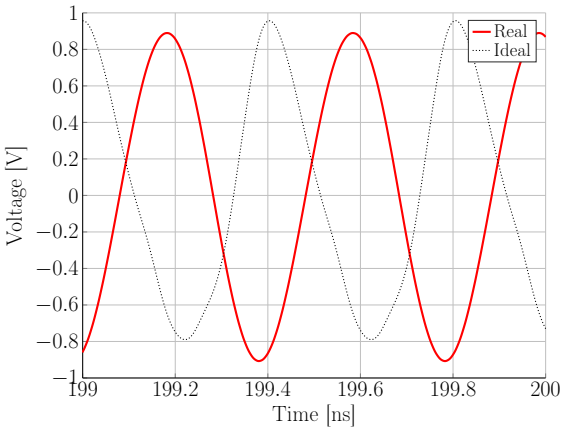


(b) Output waveform in steady-state regime

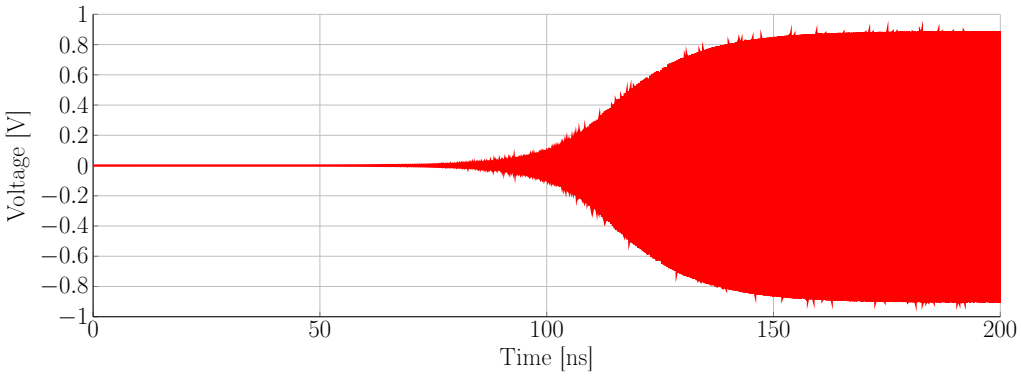


(c) Oscillation start-up

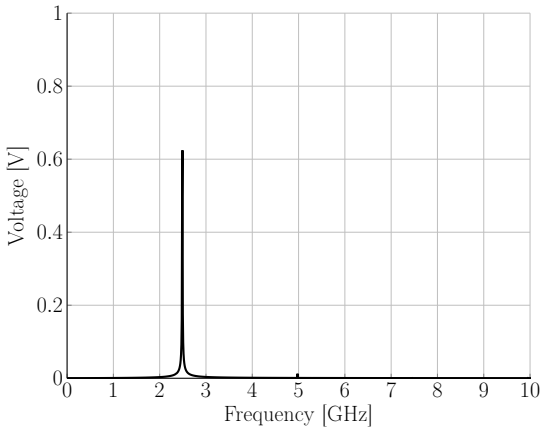


(d) FFT of time-domain output waveform

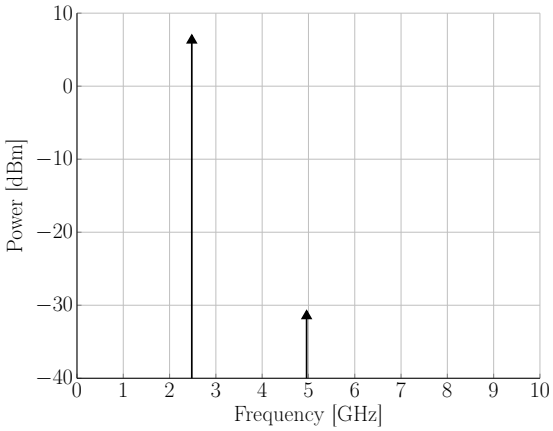


(e) HB simulation

Figure 4.12: Performance of the oscillator with real components

The output waveform of this oscillator shows a clean sinusoid (Fig. 4.12b), which outperforms the ideal schematic results. Besides, the oscillation start-up shows no signs of overshoot and the oscillation power increases smoothly. With no effect on performance, oscillation start-up is delayed, starting around 85 ns (Fig. 4.12c) and it achieves steady-state several nanoseconds later (at 180 ns). The FFT of the time-domain simulation results peaks at 2.49 GHz (Fig. 4.12d). Again, to validate the results of the transient simulation, a frequency-domain HB has been configured. HB results, shown in Fig. 4.12e, feature a 7.2 dBm oscillation at 2.48 GHz at the **OUT** node. Despite the loss of 1.3 dB of output power compared to the ideal simulations (Fig. 4.9e), second harmonic suppression is increased to 37.8 dB. The outstanding harmonic purity of the results of the real schematic might be caused by the dissipative nature of the realistic component models that have been used in the circuit and the addition of the resistance in the degenerative emitter feedback.

### Integration in CBSA bottom layer

In Fig. 3.14, a microstrip-fed AFSIW CBSA was illustrated. The oscillator prototype is designed to be connected at the end of the microstrip line shown in this figure to effectively feed the cavity and radiate. To manufacture the bottom layer, the soldering isle ($d_{isle,bot}$), the drilled hole ($d_{top}$) and the circle etched in the copper ($d_{cu,bot}$) need to be taken into account for the final layout. As shown in Fig. 4.13, the probe-feeding structure and the oscillator schematic have been combined into a single layout, which will be implemented in a Rogers© RO4350b substrate.

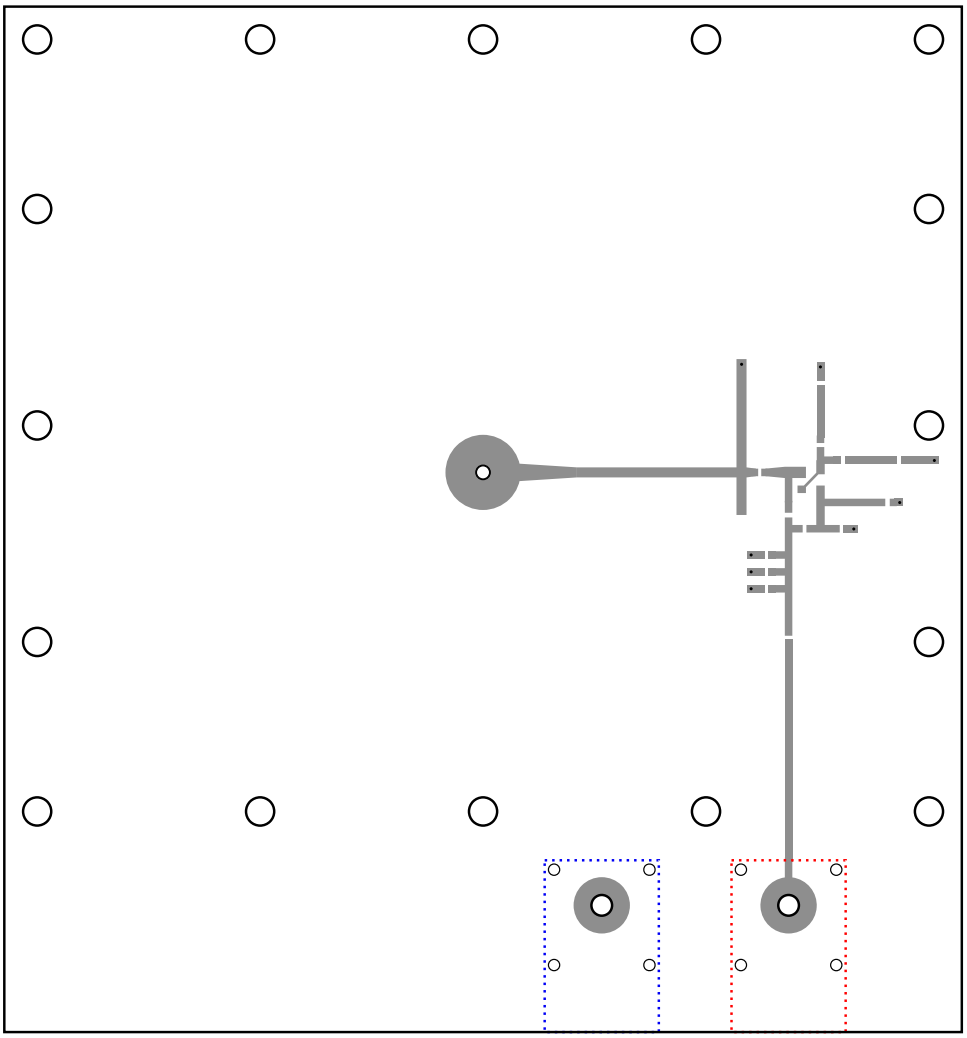

Figure 4.13: Real schematic of the oscillator integrated in the bottom layer of the AFSIW CBSA.

To guarantee a stable bias and prevent any performance degradation caused by ripple or noise on the power supply pins [50], a series of three decoupling capacitors with different values are placed at the end of the line that provides the DC voltage to the circuit. The values of these capacitors are 100 pF, 100 nF and 10 $\mu$F, which will act as a low impedance path to ground for a broad range of RF frequencies. The power supply terminals are connected to the circuit with two PCB-mounted sockets for banana jacks [51]. To make room for these

connectors, one side of the bottom layer has been extended 2 cm, and the line that connects $V_{cc}$ with the circuit has been elongated accordingly. The ground terminal of the power supply is connected to the copper layer that faces the inside cavity, which is the same ground that the RF components are referred to. Component values of the final optimized oscillator layout, together with SMD sizes and manufacturers, are shown in Table. 4.5, and a renderization of the final prototype is illustrated in Fig. 4.14.

| **Component** | **Value** | | **Manufacturer** | **Model** | **Size** |
|---|---|---|---|---|---|
| $C_{DC1}$ | 100 | pF | Murata | GRM18 | 0603 |
| $C_{DC2}$ | 100 | nF | Murata | GRM18 | 0603 |
| $C_{DC3}$ | 10 | $\mu$F | Murata | GRM18 | 0603 |
| $C_L$ | 1.8 | pF | Murata | GRM15 | 0402 |
| $C_S$ | 0.9 | pF | Kemet | CBR | 0402 |
| $C_{FB}$ | 1.8 | pF | Murata | GRM15 | 0402 |
| $R_0$ | 51 | $\Omega$ | Vishay | CRCW | 0402 |
| $R_1$ | 300 | $\Omega$ | Vishay | CRCW | 0402 |
| $R_2$ | 220 | $\Omega$ | Vishay | CRCW | 0402 |
| $R_E$ | 120 | $\Omega$ | Vishay | CRCW | 0402 |
| $R_S$ | 300 | $\Omega$ | Vishay | CRCW | 0402 |
| $L_C$ | 62 | nH | Murata | LQW15 | 0603 |
| $L_E$ | 62 | nH | Murata | LQW15 | 0603 |
| Transistor | | | Infineon | BFP193 | |
| DC Connectors | | | CLIFF | FCR7350 | |

Table 4.5: Component values of the real oscillator schematic integrated in the AFSIW CBSA.

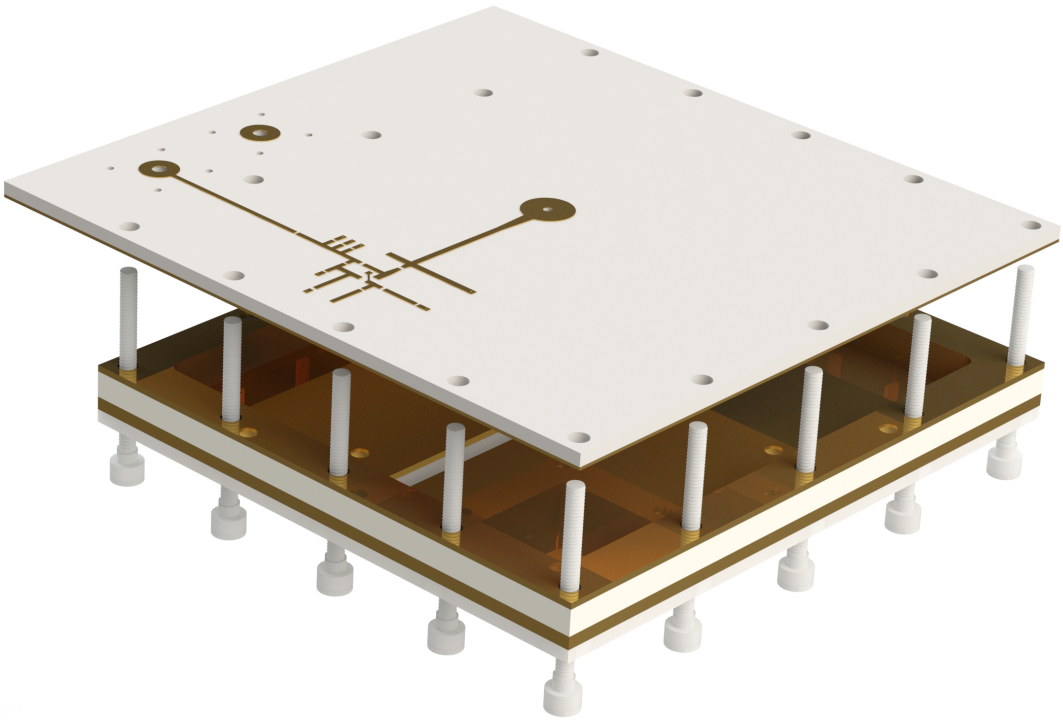

Figure 4.14: Co-designed oscillator integration in the AFSIW cavity.

## 4.5 Standalone Oscillator Prototype

To measure the output impedance of the oscillator, a standalone prototype is designed preserving the same circuit layout and component values. To connect with the measurement equipment, the footprint of a female SMA end launch connector (Southwest Microwave 292-05A [52]) is drawn at the RF output (Fig. 4.15).

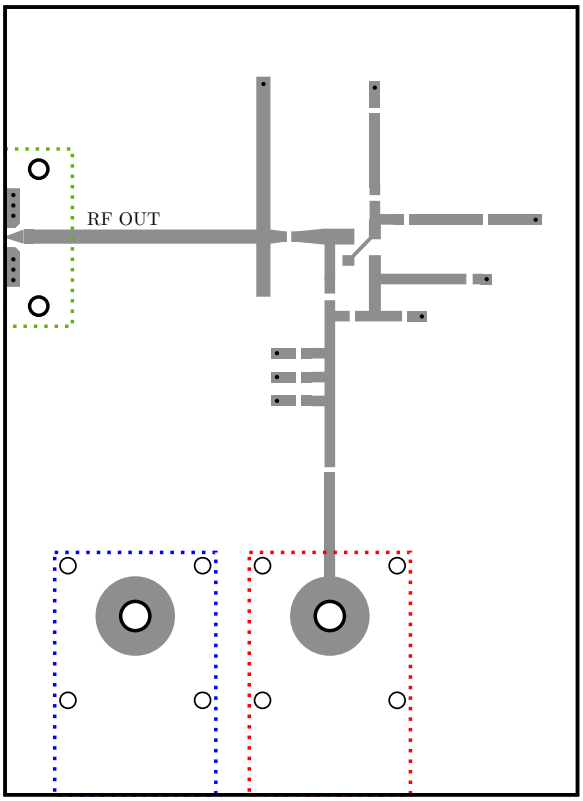


Figure 4.15: Standalone oscillator layout

In the circuit, the connector is represented by a 50 Ω port. The simulation results of this schematic show that the most unstable frequency is 2.52 GHz, although 2.45 GHz still presents $\rho_{out} = |2.7|$ (Fig. 4.16). This small deviation is due to the modification of the load, as the output matching network was designed for $Z_{ant}$ and not for a frequency-independent 50 Ω port. The output impedance, shown in Fig. 4.17, presents an negative-resistance antiresonace at the point of maximum unstability.

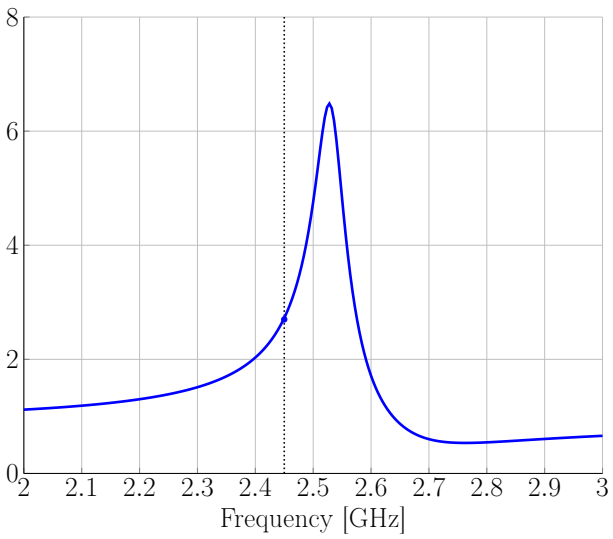


Figure 4.16: $|\rho_{out}|$ of standalone oscillator referred to a 50 Ω port

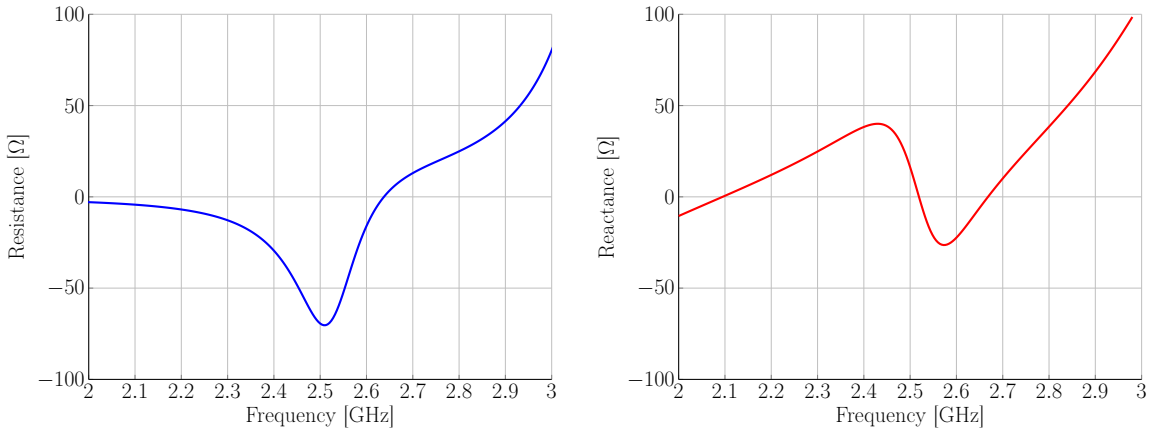


(a) Resistance

(b) Reactance

Figure 4.17: Standalone oscillator simulated output impedance.

# Chapter 5

# Measurement Results

In this chapter, the measurement results of several prototypes will be covered.

### Standalone Antenna Prototype

To measure the impedance of the CBSA, the coaxial-fed design detailed in Fig. 3.8. has been manufactured. The 50 Ω multicomp© female SMA connector has been introduced into the cavity, and properly soldered to the isle in the top layer and the pad in the bottom layer. Once the connector is properly attached to the cavity, the excess length of the inner conductor of this connector (Fig. 3.7), which acts as the probe, is cut to prevent additional backside radiation.

The prototype has been connected to a Vector Network Analyzer (VNA) with a standard SMA coaxial cable, which will measure the input impedance ($Z_{in}$) and the input reflection coefficient ($\rho_{in}$). The measurement equipment used to obtain these results is a Keysight© PNA-X, a high-performance VNA.

The input impedance and reflection coefficient of the standalone antenna prototype are shown in Fig. 5.1, as well as the simulation results from Section 3.4. The measurement results show consistency with the simulations. The same antiresonances can be observed in the reactance (Fig. 5.1b). The antiresonance at 2.35 GHz is more evident and has higher negative slope than in the simulations, which is reflected by a higher resistance (Fig. 5.1a). The antiresonance corresponding to the resonance of the $TE_{101}$ mode at 2.54 GHz is less abrupt

than the simulated one, although it still leads to a resistance maximum. At 2.45 GHz, the input impedance is $Z_{in} = 54.43 + j5.87\,\Omega$ which, referred to 50 Ω, provides an input reflection coefficient minimum: 23.06 dB (Fig. 5.1c). The −10dB-referred matched bandwidth is 60 MHz (Q= 41), from 2.415 GHz to 2.475 GHz, 10 MHz wider than the previously simulated, but still keeping 2.45 GHz as the best-matched frequency.

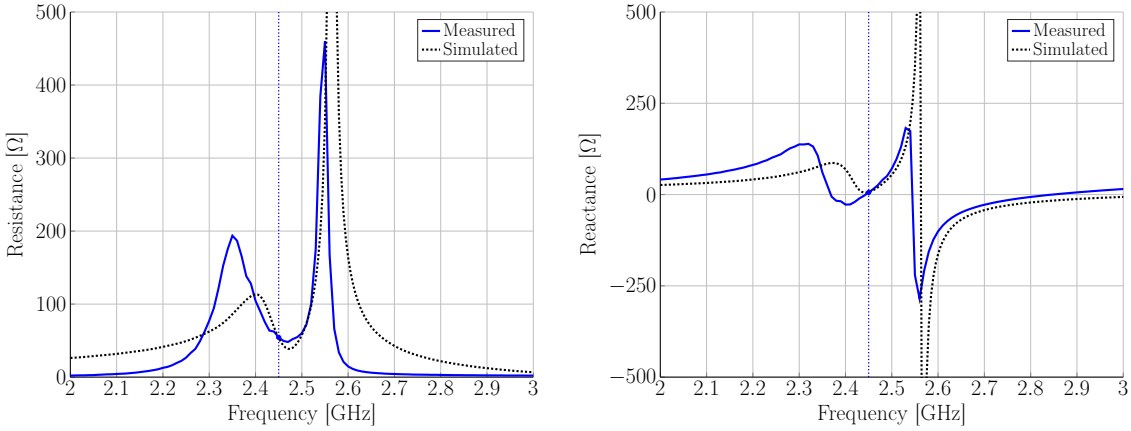


(a) Input Resistance

(b) Input Reactance

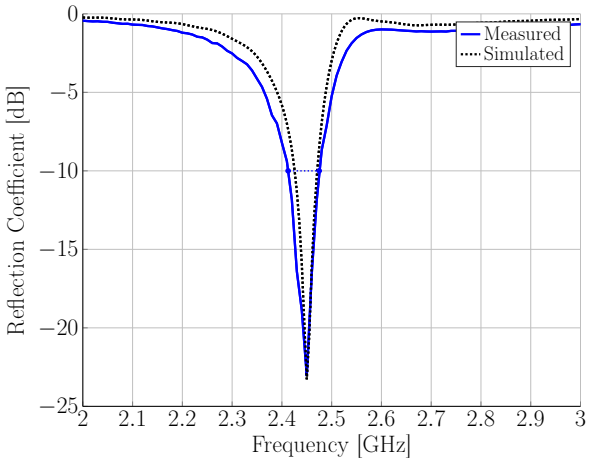


(c) Reflection Coefficient magnitude ($|\rho_{in}|$)

Figure 5.1: Standalone antenna prototype impedance measurements with PNA-X.

To completely validate the performance of the antenna, the radiation pattern is also measured. To isolate the antennas from undesired radiation and to suppress multipath propagation, the measurements are performed inside an anechoic chamber. In the measurement

set-up (Fig. 5.2) an UWB horn antenna is placed at one side of the anechoic chamber, acting as a fixed receiver. At a distance of $d_1 = 5.025\,\mathrm{m}$ — several wavelenghts away to achieve far-field conditions — the antenna under test (AUT) is placed in a rotatory positioning system, which can rotate the AUT around its $\hat{\theta}$ and $\hat{\phi}$ axes, making it possible to obtain a three-dimensional radiation pattern.

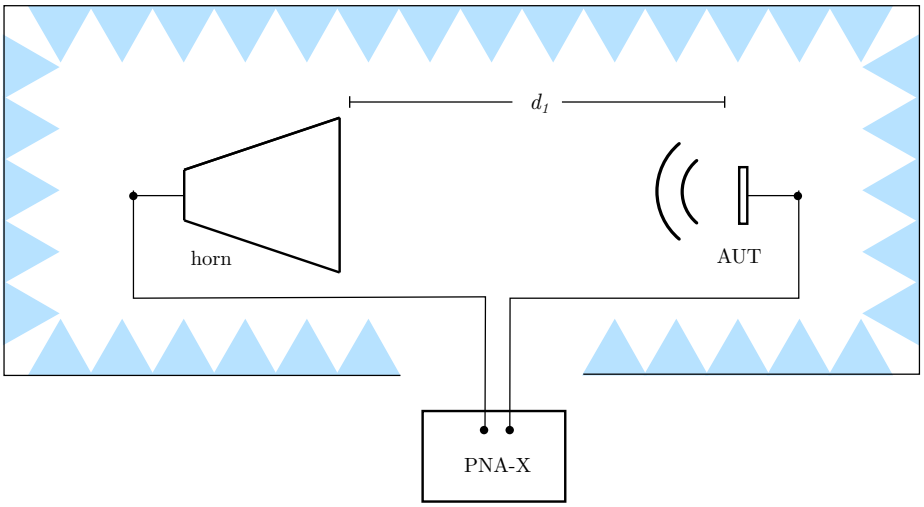


Figure 5.2: Configuration to measure the radiation pattern with the VNA.

After ensuring the antenna under test was perfectly aligned with the receiving antenna in all the possible steering directions, a full two-port calibration is executed to take the influence of the measurement set-up into consideration. The radiation pattern is measured in steps of 5° in azimuth and elevation. Overall, the measured radiation performance shows great coherence with the simulation (Fig. 5.3). Both E- and H-plane polar cuts are represented in the results, which show a gain of 7 dB in the main beam direction and 13.1 dB of FTBR. The half-power beamwidth is 60° and 95°, for the $\varphi = 0°$ and $\varphi = 90°$ polar cuts, respectively. The gain response over frequency (Fig. 5.3c) is obtained measuring the $S_{21}$. A similar ripple in the the gain is observed, which was caused by the radiation efficiency, according to the simulations (Fig. 3.12a). As it was simulated, the predominant presence of the $TE_{101}$ mode at frequencies above 2.5 GHz has an interesting effect around 2.55 GHz, where gain and radiation efficiency drastically drop to minimum values. A comparison between simulated and measured main results is shown in Table 5.1.

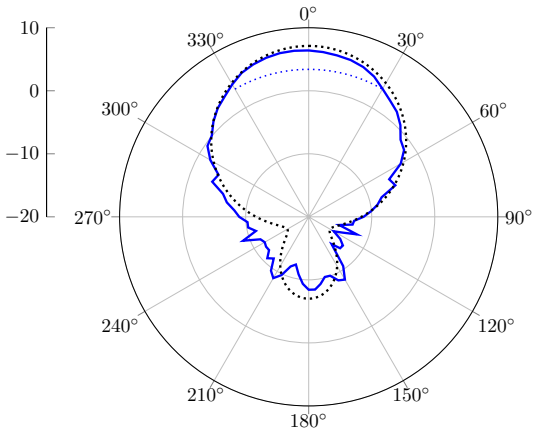


(a) $\varphi = 0°$ polar cut (H plane) at 2.45 GHz

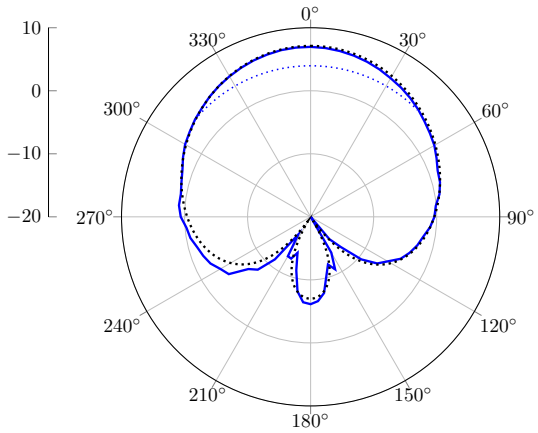


(b) $\varphi = 90°$ polar cut (E plane) at 2.45 GHz

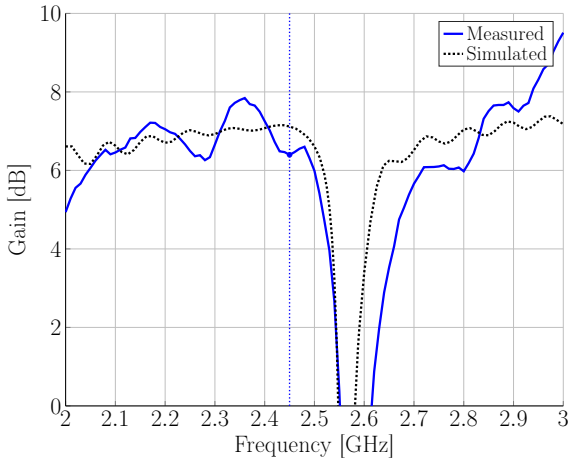


(c) Gain

Figure 5.3: Standalone antenna prototype radiation performance measurements (blue) compared to simulations (black)

| **Results** | | **Simulation** | | **Measurements** | |
|---|---|---|---|---|---|
| Input Resistance | $R_{in}$ | 53.6 | Ω | 54.4 | Ω |
| Input Reactance | $X_{in}$ | 6.3 | Ω | 5.9 | Ω |
| Reflection Coefficient | $\|S_{11}\|$ | −23.3 | dB | −23.1 | dB |
| Matched Bandwidth | BW | 50 | MHz | 60 | MHz |
| Quality Factor | Q | 49 | | 41 | |
| Gain | G | 7.1 | dB | 7 | dB |
| Angular width (E) | $\Delta\theta^{E}_{-3\text{dB}}$ | 85 | deg. | 90 | deg. |
| Angular width (H) | $\Delta\theta^{H}_{-3\text{dB}}$ | 64 | deg. | 60 | deg. |
| Front-to-Back Ratio | FTBR | 14.1 | dB | 13.1 | dB |

Table 5.1: Standalone antenna prototype simulation and measurement results at 2.45 GHz

### Standalone Oscillator Prototype

To validate the simulation results of the oscillator, a standalone oscillator prototype was designed to measure the output impedance of the oscillator, which will not be possible to measure once integrated in the AFSIW cavity. The measurement set-up is illustrated in Fig. 5.4. The equipment used for this measurement is a Keysight Fieldfox N9917A VNA. The DC voltage is applied connecting two banana jacks to a DC power supply (Keithley 2230G).

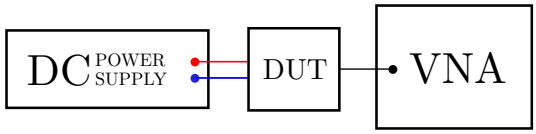


Figure 5.4: Configuration to measure the impedance of the standalone oscillator with the VNA.

The output reflection coefficient is shown in Fig. 5.5. Compared to the simulated results, the frequency of maximum unstablility has shifted to lower frequencies. This $|\rho_{out}|$ maximum, which coincides with an antiresonance (Fig. 5.6), occurs at 2.41 GHz, a 120 MHz shift in frequency. The response in impedance is similar to the simulations. The measured impedance

shows a steeper antiresonance with similar negative resistance, which mainly affects the unstable bandwidth.

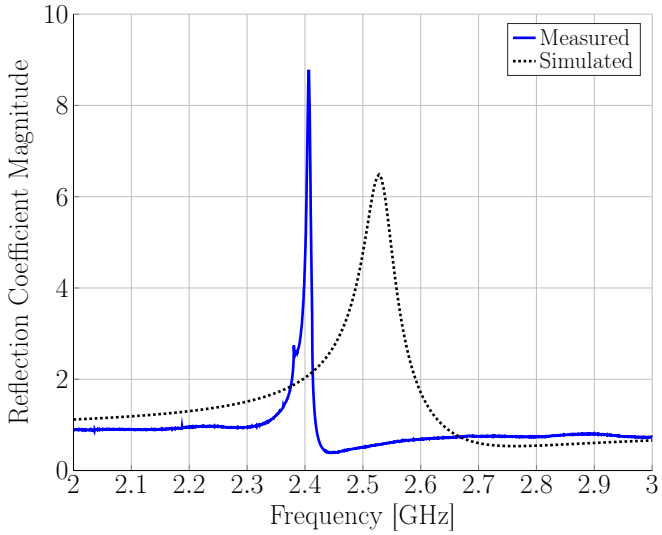


Figure 5.5: Measured $|\rho_{out}|$ of the standalone oscillator prototype

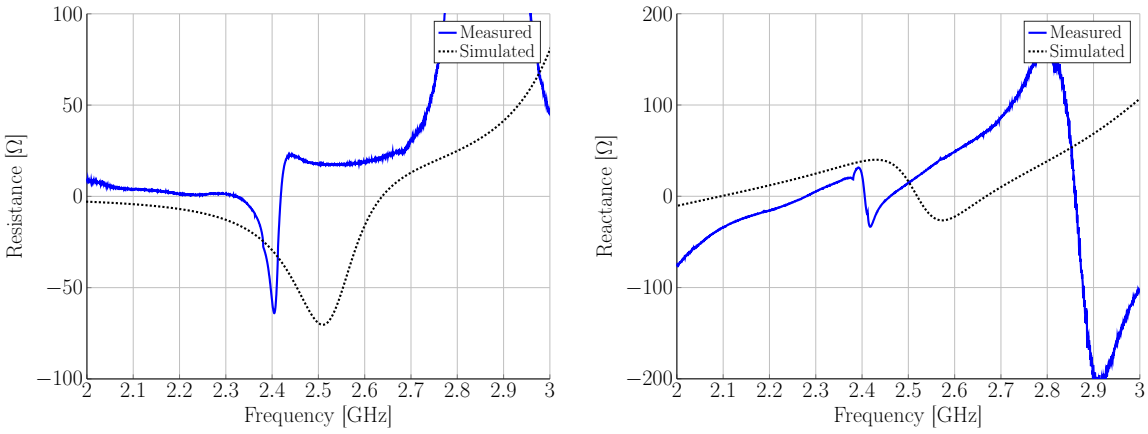


(a) Resistance

(b) Reactance

Figure 5.6: Standalone oscillator measured output impedance.

After configuring a simulation to replicate these results, it has been observed that a small increase in capacitor values provides a response closer to the measurements. The resistors

used in the circuit were measured before soldering, a small deviation in inductor values does not have a big effect on the impedance response and the microstrip transmission line manufacturing process has very small tolerances that do not cause such a difference in the response. Hence, the lower frequency of these results might be caused by a deviation from the nominal values of the employed capacitors or a high parasitic capacitance across the circuit.

### Co-designed Array Element Prototype

The design of the integrated co-designed oscillator is described in Section 4.4 and the final layout for the bottom layer of the AFSIW structure is illustrated in Fig. 4.13. The assembling process of the integrated oscillator-antenna device is the same as the standalone antenna, using the same top and middle layers. The probe excess length is cut on the top and bottom layer after soldering to each isle.

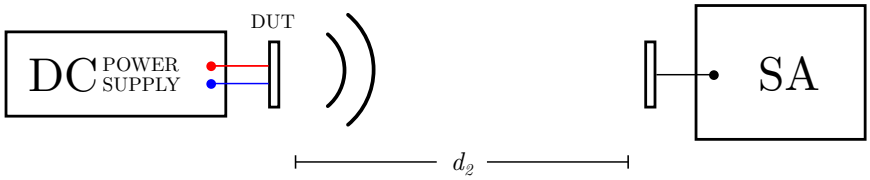


Figure 5.7: Configuration to measure the oscillation frequency and output power with the SA.

No difference in the radiation performance of the AFSIW CBSA with an integrated oscillator is expected, as its dimensions remain exactly the same. The most important results to measure from this device are the output power and the frequency of oscillation. The measurement set-up is depicted in Fig 5.7. To supply the power to the oscillator, the Keithley 2230G is used once more. Additionally, a Rhode & Schwarz Spectrum Analyzer (SA) is employed to measure the output power and $f_{osc}$. To receive power from the integrated oscillator, the standalone antenna prototype is placed a certain distance away ($d_2$) and is connected to the SA. Any undesired harmonics will be highly attenuated as they will be reflected back to the oscillator at the antenna input and, as such, the antenna acts as a high-Q filter. The oscillator's output power ($P_{osc}$) can be calculated from Friis' transmission equation:

$$P_{osc} = P_{rec} - 2G - 20\log\left(\frac{\lambda}{4\pi d_2}\right) \tag{5.1}$$

where $P_{rec}$ — the power measured in the SA — and $P_{osc}$ are in dBm units and $G$ represents the gain of the standalone antenna prototype. The response obtained from the spectrum analyzer is shown in Fig. 5.8. This final performance was obtained after a tuning process. The prototype using the components displayed in Table 4.5 produces no oscillation so, using the insights obtained with the standalone oscillator, certain component values have been adjusted in the integrated oscillator circuit to obtain an oscillation. Particularly, $C_S = 0.6\,\text{pF}$ and $C_L = 1.3\,\text{pF}$ are the new capacitors in the circuit that have led to the oscillation that can be observed in Fig. 5.8. The frequency of oscillation is 2.45 GHz, which is lower than the $f_{osc}$ of the simulated oscillator prototype, but it is the originally intended $f_{osc}$ and has better matching conditions, according to the standalone antenna performance. The received power, measured with $d_2 = 3.9\,\text{m}$ of separation between antennas, is $P_{rec} = -48.1\,\text{dBm}$, so the oscillator's output power can be calculated as:

$$P_{osc} = -48.1 - 2 \cdot 7 + 52.04 = -9.65\,\text{dBm}\,. \tag{5.2}$$

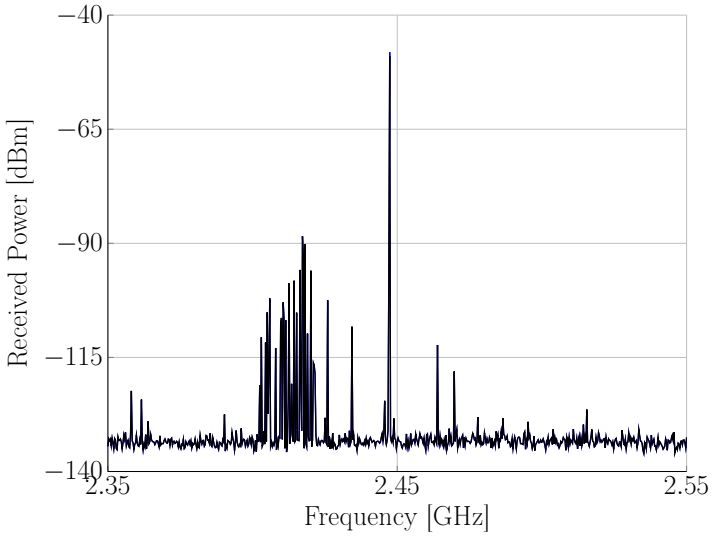


Figure 5.8: Power spectrum measured with the SA.

This oscillation power is 16.8 dB lower than the simulated in Section 4.4 (Fig. 4.12).

To guarantee that the power is not being inappropriately dissipated in the circuit, the DC operating point has been verified. $V_{CE} = 2.4\,\mathrm{V}$ and $V_{BE} = 2.7\,\mathrm{V}$ match the voltages at the transistor's terminals in the simulations, so it can be dismissed that the transistor is operating at a different DC operating point and with different characteristics. To tune the oscillator's output power, increasing $R_E$ should lead to less negative feedback, less transistor bias stability and an increased output power, whereas decreasing $R_S$ should reduce source dissipation, which has a direct effect on the oscillation conditions explained in Section 4.3. However, it has been observed that modifying these components causes small shifts in frequency with no improvement in power. One of the reasons that might cause the low $P_{rec}$, is the possibility that the transmitting CBSA, due to its sensitivity to $h_{cav}$ variations, is not matched at 2.45 GHz and there are high mismatch losses. The presence of high power harmonics can also be the reason why most of the power is not delivered at the operating frequency. However, the high out-of-band mismatch losses and the low gain at these frequencies due to higher-order electric field modes inside the slot would make the overtones undistinguishable from co-existing technologies (such as 5 GHz Wi-Fi).

# Chapter 6

# Conclusions and Future Work

The goal of this master's dissertation was to design an antenna array element operating at the 2.45 GHz ISM band, with a phase distribution controlled by injection-locked coupled oscillators to achieve phase shifter-less beam steering. A cost-effective oscillator coupling mechanism was presented, based on aperture-coupled air-filled SIW cavities. To obtain an array element prototype, the design was divided in two modules: antenna and co-designed oscillator. These two modules, given the characteristics of SIW cavities, were to be integrated in opposite sides of the same AFSIW structure, minimizing the influence between them.

To obtain outstanding radiation performance and seamless integration with the SIW cavity coupling mechanism, a CBSA was designed as the antenna module. Supporting a hybrid mode to maximize radiation efficiency, more than $\eta_{rad} = 85\%$ is observed in the measurement results of the standalone AFSIW CBSA in a broad range of frequencies around 2.45 GHz and, in particular, 95% at the operating frequency. The antenna features a $G = 7$ dB omnidirectional beam with broad half-power beamwidths, and reflects the self-shielding quality of CBAs showing 13 dB of FTBR.

The oscillator module was designed to be integrated on the bottom layer of the AFSIW cavity, on the opposite side of the slot. The device was designed as a negative resistance oscillator, that is, a common-base amplifier was appropriately destabilized to present negative resistance at both input and output ports. The oscillator was carefully co-designed to guarantee start-up and steady-state conditions using an oscillator-ready version of the AFSIW CBSA as a load. Simulations predicted a 7.2 dBm oscillation at 2.48 GHz with excellent

harmonic purity ($> 38\,\mathrm{dB}$). Notwithstanding the fact that the measurement results of a standalone version of the oscillator module showed an excess capacitance in the circuit, this was successfully compensated by manual tuning of the circuit capacitors. The oscillator integrated in the AFSIW CBSA, which represents the final array element originally intended, features an oscillation at $2.45\,\mathrm{GHz}$. However, despite the numerous attempts to obtain a different outcome, the calculated oscillator's output power is $-9.65\,\mathrm{dBm}$, almost $17\,\mathrm{dB}$ of difference with the simulations.

The designed CBSA showed a steep impedance response and somewhat fragile matching conditions. As a result, the antenna prototypes presented high sensitivity to height variations, so that any subtle pressure or soldering inaccuracy would shift the operating frequency of the antenna, although with a constant matched bandwidth. This impedance behavior did also affect the oscillator response, and fine-tuning the oscillating frequency became a burdensome task. Despite the inability to measure the final device, the sensitivity of the CBSA in the assembling process suggests that the oscillator is working in conditions different than the simulated ones, which could account for the substantial deviation in output power. Non-effective harmonic suppression is another plausible cause of power loss, although measurements of the standalone oscillator do not show significant presence of overtones.

Future developments in the same line of work should emphasize the prevention of any possible structural unstability in the assembled AFSIW structure. A more sophisticated solution than a teflon piece inside the cavity would prevent some of the simulation and measurement discrepancies from happening. Besides, matching the antenna to a less steep region — at the expense of bandwidth — would allow for some error margin. Regarding the oscillator, once the CBSA response is stable and fairly predictable, finding ways to immunize the oscillator from the effects of the steep CBSA impedance out of the desired operating band will hamper potential out-of-band oscillations. Besides, filtering the impedance of the CBSA to work just with the intended frequency of operation would simplify the oscillator's internal behavior and ease the tuning process at the same time.

Once both oscillator and antenna are integrated and working with a proper output power, an array can be safely designed. Having a predictable output power is important to design the appropriate coupling between cavities, which will define the phase difference between antennas. Either way, the design of the array requires thorough understanding of the bidirectional coupling between neighboring array elements, as steady-state phase relationships become difficult to calculate, so adding some manual tuning ability to the coupling mechanism,

instead of having a fixed coupling, would certainly be helpful. As long as the oscillating frequency and output power are under control, further developments on this matter will eventually lead this array element to a fully functional phase shifter-less beam steering array.

# Bibliography


[1] Ma, Mark T. Theory and application of antenna arrays. John Wiley & Sons, 1974.

[2] Rabinovich, Victor, and Nikolai Alexandrov. Antenna arrays and automotive applications. Springer Science & Business Media, 2012.

[3] York, Robert A., and Tatsuo Itoh. "Injection-and phase-locking techniques for beam control [antenna arrays]." IEEE Transactions on Microwave Theory and Techniques 46.11 (1998): 1920-1929.

[4] Yan, Sheng-Hong, and Tah-Hsiung Chu. "A beam-steering antenna array using injection locked coupled oscillators with self-tuning of oscillator free-running frequencies." IEEE Transactions on Antennas and Propagation (2008): 2920-2928.

[5] Huynen, Martijn. "EMC-Aware Design of a Low-Cost Receiver Circuit under Injection Locking and Pulling." Chapters 2-4. (2014).

[6] Adler, Robert. "A study of locking phenomena in oscillators." Proceedings of the IEEE 61.10 (1973): 1380-1385.

[7] Liao, P., and R. A. York. "A new phase-shifterless beam-scanning technique using arrays of coupled oscillators." IEEE transactions on microwave theory and techniques 41.10 (1993): 1810-1815.

[8] Stephan, K. A. R. L. D., and W. I. L. L. I. Morgan. "Analysis of interinjection-locked oscillators for integrated phased arrays." IEEE transactions on antennas and propagation 35.7 (1987): 771-781.

[9] Stephan, Karl D. "Inter-injection-locked oscillators for power combining and phased arrays." IEEE Transactions on Microwave Theory and Techniques 34.10 (1986): 1017-1025.

[10] York, Robert A. "Nonlinear analysis of phase relationships in quasi-optical oscillator arrays." IEEE Transactions on Microwave Theory and Techniques 41.10 (1993): 1799-1809.

[11] Alexanian, Angelos, Heng-Chia Chang, and Robert A. York. "Enhanced scanning range of coupled oscillator arrays utilizing frequency multipliers." Antennas and Propagation Society International Symposium, 1995. AP-S. Digest. Vol. 2. IEEE, 1995.

[12] Pogorzelski, Ronald J., and Apostolos Georgiadis. Coupled-oscillator based active-array antennas. Vol. 11. John Wiley & Sons, 2012.

[13] Moussounda, Renaud. "Analysis and design of coupled-oscillator arrays for microwave systems." The Ohio State University, 2014.

[14] Liao, P., and R. A. York. "A 1 Watt X-band power combining array using coupled VCOs." Microwave Symposium Digest, 1994., IEEE MTT-S International. IEEE, 1994.

[15] York, Robert A., Peter Liao, and Jonathan J. Lynch. "Oscillator array dynamics with broadband N-port coupling networks." IEEE Transactions on Microwave Theory and Techniques 42.11 (1994): 2040-2045.

[16] Filatrella, Giovanni, Niels Falsig Pedersen, and Kurt Wiesenfeld. "High-Q cavity-induced synchronization in oscillator arrays." Physical Review E 61.3 (2000): 2513.

[17] Zhong, Cuilin, et al. "Ka-Band Substrate IntegratedWaveguide Gunn Oscillator." IEEE Microwave and Wireless Components Letters 18.7 (2008): 461-463.

[18] Collado, Ana, et al. "Optimized design of substrate integrated waveguide cavity based oscillators." Feedback 12.6.89 (2010): 13-4.

[19] Giuppi, F., et al. "Hybrid nonlinear and electromagnetic design of an active oscillator SIW cavity backed slot antenna." Applied Computations Electromagnetics Society Symposium. (ACES), Tampere, Finland. 2010.

[20] Giuppi, F., et al. "An X band, compact active cavity backed patch oscillator antenna using a substrate integrated waveguide (SIW) resonator." IEEE Antennas and Propagation Society International Symposium (APSURSI). 2010.

[21] Bozzi, Maurizio, Anthimos Georgiadis, and Kaijie Wu. "Review of substrate-integrated waveguide circuits and antennas." IET Microwaves, Antennas & Propagation 5.8 (2011): 909-920.

[22] Giuppi, F., et al. “Active antenna oscillator systems in substrate integrated waveguide (SIW) technology." IEEE Proceedings of the Fourth European Conference on Antennas and Propagation (EuCAP). 2010.

[23] Chen, Chih-Jung, and Tah-Hsiung Chu. “Design of a 60-GHz substrate integrated waveguide Butler matrix—A systematic approach.” IEEE Transactions on Microwave Theory and Techniques 58.7 (2010): 1724-1733.

[24] Zheng, M., et al. “Cavity control of active integrated antenna oscillators.” IEEE Proceedings on Microwaves, Antennas and Propagation 148.1 (2001): 15-20.

[25] Ghosh, Basudeb, Sachendra N. Sinha, and M. V. Kartikeyan. Fractal Apertures in Waveguides, “Conducting Screens and Cavities: Analysis and Design.” Vol. 187. Springer, 2014.

[26] Chandra, Rohit, and Axel Von Arbin. “Cavity-backed slot antennas for wireless portable devices.” IEEE 2016 10th European Conference on Antennas and Propagation (EuCap).

[27] A. Hadidi, M. Hamid, Aperture field and circuit parameters of cavity-backed slot radiator. IEEE Proceedings Microwaves, Antennas and Propagation. Pt. H. 136(2):139–146 (1989)

[28] G. Luo, T. Wang, and X. Zhang, “Review of Low Profile Substrate Integrated Waveguide Cavity Backed Antennas”, International Journal of Antennas and Propagation, 2013.

[29] Cardama, Ángel, et al. Antenas. Edicions de la Universitat Politècnica de Catalunya, (2002).

[30] Pozar, David M. Microwave engineering. John Wiley & Sons, 2009.

[31] Luo, Guo Qing, et al. “Planar slot antenna backed by substrate integrated waveguide cavity.” IEEE Antennas and Wireless Propagation Letters 7 (2008): 236-239.

[32] Luo, Guo Qing, et al. “Bandwidth-enhanced low-profile cavity-backed slot antenna by using hybrid SIW cavity modes.” IEEE transactions on Antennas and Propagation 60.4 (2012): 1698-1704.

[33] Ghiotto, Anthony, et al. “Air-filled substrate integrated waveguide—A flexible and low loss technological platform.” IEEE 13th International Conference on Advanced Technologies, Systems and Services in Telecommunications (TELSIKS), 2017.

[34] Parment, Frédéric, et al. “Air-filled substrate integrated waveguide for low-loss and high power-handling millimeter-wave substrate integrated circuits.” IEEE Transactions on Microwave Theory and Techniques 63.4 (2015): 1228-1238.

[35] Van den Brande, Quinten, et al. “Highly-efficient impulse-radio ultra-wideband cavity-backed slot antenna in stacked air-filled substrate-integrated-waveguide technology.” IEEE Transactions on Antennas and Propagation (2018).

[36] M. Nanda Kumar and T. Shanmuganantham “Microstrip feed substrate integrated waveguide cavity slot antenna for 60GHz applications” International Conference on Communication and Signal Processing (ICCCSP), 2017.

[37] Joubert, Johan, et al. “CPW-fed cavity-backed slot radiator loaded with an AMC reflector.” IEEE Transactions on Antennas and Propagation 60.2 (2012): 735-742.

[38] Lertwiriyaprapa, Titipong, C. Phongcharoenpanich, and M. Krairiksh. “Analysis of radiation characteristics of a probe fed rectangular cavity-backed slot antenna with finite-size ground plane.” IEEE Antennas and Propagation Society International Symposium, 2000. Vol. 2.

[39] Waterhouse, Rod. Microstrip patch antennas: a designer’s guide. Springer Science & Business Media, 2013.

[40] Mayhew-Ridgers, Gordon, Johann W. Odendaal, and Johan Joubert. “Efficient full-wave modeling of patch antenna arrays with new single-layer capacitive feed probes.” IEEE Transactions on Antennas and Propagation 53.10 (2005): 3219-3228.

[41] “FR402 Tetrafunctional Epoxy Laminate and Prepreg,” Technical Report, Isola, 2018.

[42] “RO4000 Series High Frequency Circuit Materials,” Technical Report, Rogers corporation, 2018

[43] Kashyap, Ravindra S. “Waveguide resonators.” Term paper report, Dept. of Electrical Engineering, Indian Institute of Technology, Bombay.

[44] Loy, Matthew, Raju Karingattil, and Louis Williams. “ISM-band and short range device regulatory compliance overview.” Texas Instruments (2005).

[45] ETSI. 300 328 V1. 9.1. Electromagnetic compatibility and Radio spectrum Matters (ERM). 2015.

[46] Gilmore, Rowan, and Les Besser. Practical RF Circuit Design for Modern Wireless Systems: Active Circuits and Systems, Volume 2. Artech House, 2003.

[47] Dye, Norman, and Helge Granberg. Radio frequency transistors: principles and practical applications. Elsevier, 2001.

[48] F. W. L. Kung, "Lesson 9 - oscillator design," April 2012, open lecture notes.

[49] "BFP193 Low Noise Silicon Bipolar RF Transistor" Technical Report, Infineon, 2018.

[50] Ardizzoni, John. "A practical guide to high-speed printed-circuit-board layout." Analog Dialogue 39.9 (2005): 1-6.

[51] "FCR7350 4mm PANEL SOCKET S16N-PC" Technical Report, Cliff, 2018.

[52] "292-05A-5 SMA Jack Female End Launch Connector" Technical Report, Southwest Microwave, 2018.